

24 h in tumor xenografts was observed. We also found that glycosaminoglycans played a key role in accumulation in tumors.

To assess the applicability of r8 for cancer therapy, a conjugate of doxorubicin with r8 (4 mg doxorubicin/kg) was prepared, which effectively suppressed tumor proliferation without decreasing mouse weight after intravenous injection. A higher dose of doxorubicin (6 mg/kg) was necessary to obtain the same extent of tumor growth suppression without conjugation to r8, but this was accompanied by significant weight loss.

2. Materials and methods

2.1. Peptide synthesis and fluorescent labeling

All the peptides employed in this study were chemically prepared by the 9-fluorenylmethyloxycarbonyl solid-phase peptide synthesis on a Rink amide resin as already described [27]. The amino acid derivatives and Rink amide resin (TGS-RAM) were purchased from the Peptide Institute (Osaka, Japan) and Shimadzu Biotech (Kyoto, Japan). Each arginine-rich peptide was designed to have a cysteine or glycyl cysteine amide at the C-terminus for the fluorescent labeling. Deprotection of the peptides and cleavage from the resin were conducted by treatment with a trifluoroacetic acid/ethanedithiol mixture (95:5) at room temperature for 3 h. Fluorescent labeling was conducted by treatment with 1.5 equivalents of Alexa Fluor 660 (alexa660) C2 maleimide sodium salt (Invitrogen, Eugene, OR, USA) in a dimethyl formamide/methanol mixture (1:1) for 1.5 h at room temperature followed by reverse-phase high-performance liquid chromatography purification. The structures of the synthesized peptides were confirmed by matrix-assisted laser desorption ionization time-of-flight mass spectrometry. Concentration of each peptide was adjusted based on the molar extinction coefficient at 668 nm ($112,000 \text{ cm}^{-1} \text{ M}^{-1}$) [28].

2.2. Cell culture

Human cervical cancer-derived HeLa cells were purchased from the Riken BRC Cell Bank (Ibaraki, Japan) and cultured in α -minimal essential medium (α -MEM) containing 10% heat-inactivated bovine serum (Invitrogen). Chinese hamster ovary (CHO) cells [CHO-K1 cell lines, wild type; pgsA-745 (A-745) cell lines, all glycosaminoglycan deficient] were purchased from the American Type Culture Collection (Manassas, VA, USA), and cultured in an F-12 nutrient mixture (Ham's F-12) containing 10% heat-inactivated fetal bovine serum (Biological Industries, Kibbutz Beit Haemek, Israel). Cells were grown on 100-mm dishes and incubated at 37 °C under 5% CO₂.

2.3. Tumor-xenografted nude mouse

Animal studies were conducted in accordance with our institutional guidelines, and the experimental procedures were approved by the Kyoto University Animal Care Committee.

Female BALB/c nu/nu mice at 5 weeks of age were purchased from Japan SLC (Hamamatsu, Japan). HeLa (1.0×10^6 cells), CHO-K1 (4.0×10^6 cells), and A-745 (4.0×10^6 cells) were subcutaneously implanted into the shoulder of separate mice. The tumors were allowed to grow for ~2 weeks (HeLa) and ~4 weeks (CHO-K1 and A-745) to a volume of ~150 mm³, then the *in vivo* studies were conducted.

2.4. *In vivo* and *ex vivo* fluorescent imaging

In vivo fluorescent imaging was conducted using an IVIS Spectrum System (Xenogen, CA, USA) at 1, 3, 6, 12, and 24 h after the tumor-xenografted mice were injected with alexa660-labeled CPPs (3 nmol in PBS) into the tail vein. During the imaging, the mice were kept

on the imaging stage under anesthesia with 2.5% isoflurane gas in flowing oxygen. Fluorescent signals were detected using emission and excitation filters of 640 and 700 nm, respectively. *Ex vivo* imaging was also performed using the IVIS Spectrum System. When the mice were sacrificed at 24 h after the injection of the alexa660-labeled CPPs, fluorescent signals of each organ and the tumor were detected similar to the *in vivo* imaging.

2.5. Conjugation of CPPs to doxorubicin

The doxorubicin-maleimide compound was first prepared following the procedures reported by Furgeson et al. [29]. Doxorubicin (0.02 mmol) was dissolved in 5 mL of anhydrous methanol. *N*-(β -maleimidopropionic acid) hydrazide, trifluoroacetic acid salt (Pierce, Rockford, IL, USA) (0.04 mmol) was dissolved in 250 μ L of anhydrous methanol and added to the doxorubicin solution. Two drops of trifluoroacetic acid were added to catalyze the Schiff-base formation of the hydrazide with the 13-keto position of the doxorubicin. The mixture was stirred at 20 °C for 4 h. Excess methanol was removed by rotary evaporation and the sample was purified by precipitation in anhydrous ethyl acetate. The purified samples were characterized by ¹H NMR and fast atom bombardment mass spectrometry.

The conjugation of the non-fluorescently labeled r8 [(D-Arg)₈-Gly-Cys-amide] with doxorubicin-maleimide was conducted by the treatment of the peptides with 1.5 equivalents of doxorubicin-maleimide in a dimethyl formamide/methanol mixture (1:1) for 1.5 h at room temperature followed by reverse-phase high-performance liquid chromatography purification. The structures of the synthesized peptides were confirmed by matrix-assisted laser desorption ionization time-of-flight mass spectrometry.

2.6. Tumor proliferation assay *in vivo*

After calculating tumor size (day 0; length \times (width)²/2, [24,30]), tumor-bearing mice were injected with the test compounds (2–6 mg/kg/day, dissolved in PBS) into the tail vein three times at 24 h intervals. After initial administration, tumor size was again estimated at 48 or 72 h intervals for up to 20 days. Body weights were measured similarly before and after injection of the test compounds. The average body weight of the mice was ~20 g; thus, the dose of 4 mg doxorubicin/kg corresponded to ~150 nmol r8-doxorubicin conjugate.

2.7. Cell viability

Cell viability was examined by MTT [3-(4,5-dimethylthiazol-2-yl)-2,5-diphenyltetrazolium bromide] assay as previously described [31]. Briefly, cells (5.0×10^3 cells/well) were cultured in 96-well microplates in α -MEM with 10% heat-inactivated bovine serum for 24 h. The cells were then incubated with the compounds (total volume, 50 μ L) at 37 °C under 5% CO₂ for 24 h. MTT in PBS (0.05 mg/10 μ L) was added to the above medium, and the cells were further incubated for 4 h. The precipitated MTT formazan was dissolved overnight in 0.04 N HCl in isopropanol (100 μ L). The absorbance at 570 nm (A570) was then measured. Cell viability was expressed as the A570 ratio of the test compound-treated cells compared with cells incubated in the absence of the compounds.

2.8. Confocal microscopy and immunostaining

CHO-K1 cells and A-745 cells (4.0×10^5 cells/well) were plated on 35-mm glass-bottomed dishes (Iwaki, Tokyo, Japan) and cultured in Ham's F-12 medium containing 10% heat-inactivated fetal bovine serum for 48 h. After complete adhesion, the cells were washed with serum-free Ham's F-12 medium, and then the cells were incubated at 4 °C for 15 min in the medium (200 μ L). The cells were

treated with anti-heparan sulfate antibody (10E4 epitope) (Seikagaku corporation, Tokyo, Japan) (1 $\mu\text{g}/200\ \mu\text{L}$) at 4 °C for 30 min in serum-free Ham's F-12 medium, followed by washing the cells with PBS and the treatment of Alexa Fluor 488 (alexa488) goat anti-mouse IgM antibody (Invitrogen) (1 $\mu\text{g}/200\ \mu\text{L}$) at 4 °C for 30 min in serum-free Ham's F-12 medium. Distribution of the fluorescent signals on the cell membranes was analyzed using an FV300 confocal scanning laser microscope (Olympus) equipped with a $\times 60$ objective.

3. Results

3.1. Biodistribution of typical CPPs in tumor-xenografted mice after intravenous administration

We first examined the biodistribution of typical CPPs, including Tat peptide (amino acids 48–60 of HIV-1 Tat protein) [11], penetratin (Pen, derived from amino acids 43–58 of the Antennapedia homeoprotein) [32], and octaarginine (R8) composed of L-arginine [12,13] (Fig. 1A) in the tumor-xenografted nude mice with HeLa cells (derived from cervical cancer cells). These CPPs have been used as representative membrane-permeable carriers for efficient intracellular delivery [14]. For optical imaging, these CPPs were labeled with alexa660 at the cysteine residue located at their C-termini (Fig. 1A). Alexa660 may also be considered a model of a small molecular bioactive compound or anti-tumor agent to be delivered with the help of these CPPs. The GC peptide was used as a control to assess the effect of alexa660 on the biodistribution. Fluorescence images of mice 24 h after intravenous injection of the peptides (3 nmol) demonstrated that among the CPPs tested R8 accumulated the most (Fig. 1B). The distribution of each peptide in tumors and other organs was further analyzed in mice sacrificed 24 h after injection of each peptide (Fig. 1C). Compared to the control GC peptide, these CPPs showed relatively high accumulation in the kidney, liver, and lung. Interestingly, although the accumulations of Tat and Pen were only slightly different from that of the control GC peptide in tumors, that of R8 was significantly higher than the other peptides. In addition, compared to the control peptide, there were no significant differences in the accumulation of these CPPs in the blood, spleen, pancreas, heart, muscle, or brain at 24 h after administration. These results prompted us to study the biodistribution and tumor accumulation of the oligoarginine peptides further.

3.2. Effects of the number and configuration of arginine residues on the biodistribution of oligoarginine peptides in vivo

The number of arginine residues plays a critical role in determining the method of internalization and the internalization efficiencies of oligoarginine peptides. Thus, we synthesized alexa 660-labeled R2, R8, R12, and R16 peptides (Fig. 2A), and analyzed their biodistributions using an *in vivo* optical imager (Fig. 1B). R8 showed the highest accumulation in tumors at 24 h after administration (Fig. 2B). Substitution of peptide sequences by their D-enantiomers often increases the resistance of peptides to degradation by proteases. Thus, we prepared the D-enantiomer of the R8 peptide (r8) and examined its biodistribution and the extent of its accumulation in tumors. As a reference, the behavior of r12 (the D-enantiomer of R12) was also studied. Marked accumulation of r8 was observed in the tumor xenografts (Fig. 2B); it was almost three times higher than that of R8, and nine times higher than that of the control GC peptide (Fig. 2C). High accumulation of r12 was also observed, but it was similar to that of R8 and significantly less than that of r8. Interestingly, the degree of accumulation was not proportional to the internalization efficiencies of these compounds in cultured cells, in which the r12 peptide showed the highest internalization efficiency (Fig. S1 in Supplementary Content).

A GC: GC*-amide
Tat: GRKKRRQRRRPPQ-C*-amide
Pen: RQIKIWFQNRRMKWKK-GC*-amide
R8: RRRRRRRR-GC*-amide

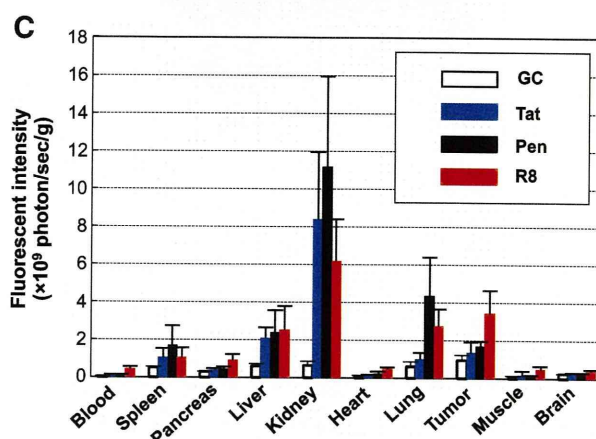
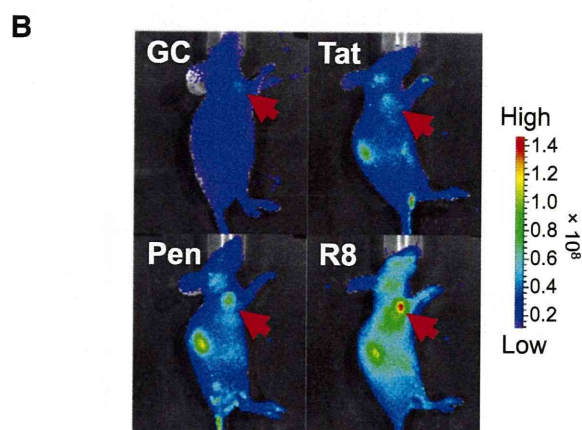


Fig. 1. Biodistribution of fluorescently labeled CPPs intravenously administered into tumor-xenografted mice. (A) Structures of arginine-rich CPPs employed in this study. For the fluorescent labeling with alexa660, a cysteine (C) amide or glycyL-cysteine (GC) amide segment is attached to each peptide. The GC peptide that does not contain the CPP segments was employed as a control. C* denotes the alexa660-labeled cysteine. (B) *In vivo* fluorescent imaging of tumor-xenografted mice at 24 h after intravenous injection of alexa660-labeled CPPs (3 nmol). Red arrows show tumor regions. (C) Fluorescent intensity of tumor and each organ. The mice were sacrificed at 24 h after the injection of the alexa660-labeled GC (white), Tat (blue), penetratin (black), and R8 (red) peptides (3 nmol each), and then the fluorescent intensity of the tumor and each organ was analyzed using the IVIS Spectrum System. Data represent the average (\pm standard deviation (SD)) of five animals.

3.3. Time-course of accumulation of oligoarginines in tumors after administration

To study the mechanism of accumulation of r8 in tumor xenografts further, the intensities of r8-alexa660 signals in tumor xenografts were analyzed sequentially together with the other oligoarginine peptides (Fig. 3). Data were obtained at 1, 3, 6, 12, and 24 h after injection of the peptide in mice, and the accumulation of the peptide in tumors and in muscle (control organ) was analyzed using optical imaging.

Compared to all other peptides, there was a marked accumulation of r8 in tumors at 1 h after injection, which decreased to $\sim 30\%$ at 24 h (Fig. 3D). The level of accumulation of r12 at 1 h after administration was almost half that of r8 (Fig. 3E). A time-dependent decrease in the

A L-forms of oligoarginine
 Rn : Rn-GC*-amide (n = 2, 8, 12, 16)
D-forms of oligoarginine
 rn : rn-GC*-amide (n = 8, 12)

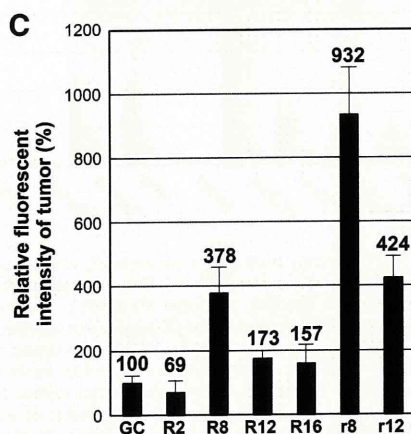
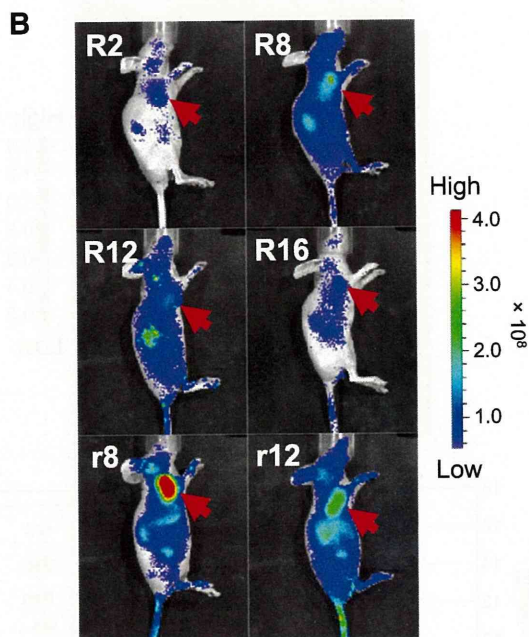


Fig. 2. Tumor accumulation of fluorescently labeled oligoarginine peptides intravenously administered into tumor-bearing mice. (A) Structures of oligoarginine peptides bearing the GC-amide segment at the C-termini for the labeling with alexa660. R and r represent L- and D-arginines, respectively. C* denotes alexa660-labeled L-cysteine. (B) *In vivo* fluorescent imaging of tumor-xenografted mice at 24 h after intravenous injection of alexa660-labeled oligoarginine peptides (3 nmol each). Red arrows represent tumor xenografts. (C) Relative fluorescent intensity of tumor xenografts in B. The fluorescent intensity in tumor xenografts of mice treated with each peptide was adjusted based on the intrinsic fluorescence intensity before peptide administration. Data represent the average (\pm SD) of five animals.

accumulation level was also observed for r12, yielding a ~20% retention of the r12 signal at 24 h. R12 showed similar accumulation to r12 at 1 h after administration. However, a steeper decrease in the signal level was observed for R12 (Fig. 3C). R8 had a less intense signal in tumors than did R12 at 1 h after administration, but it decreased at a slower rate than did R12 and at 24 h the signal was

slightly higher than that of R12. Although GC-treated mice also showed a slight increase in fluorescence signal in tumors at 1 h after administration, the signal quickly decreased to the control level (Fig. 3A). The signals of peptides were significantly lower in muscle than in tumors at 1 h after administration, and the signals in muscle returned to control levels at 24 h (Fig. 3).

Time-course analyses showed that there was significantly more (~5-fold) r8 than R8 in blood at 1 h after intravenous injection. However, at 6 h after injection, r8 decreased to almost baseline levels, at which point levels were comparable to those of R8, suggesting higher retention of r8 in the blood (Supplementary Content Fig. S2).

3.4. Accumulation of oligoarginine peptides in organs

Twenty-four hours after intravenous administration of each fluorescently labeled oligoarginine peptide (3 nmol), the mice were sacrificed and fluorescence intensities in isolated organs and tumors were analyzed using an optical imaging system (Fig. 4). Among the CPPs tested, the signal of r8 in tumors was highest, as observed in the live imaging (Fig. 2). Similar accumulation of r8 in tumors was also observed in the liver and kidney (Fig. 4). Among the peptides tested, r12 accumulated the most in the liver (Fig. 4B). Compared to peptides composed of L-arginine, the retention of those with D-enantiomers was higher in tumors, presumably because of their resistance to proteases prior to their accumulation in the tumors [33].

3.5. Importance of glycosaminoglycans in the accumulation of r8 peptide in tumors

Membrane-associated proteoglycans, consisting of membrane proteins attached to sulfated disaccharide units called glycosaminoglycans (GAGs), play an important role in promoting the cellular uptake of arginine-rich CPPs [34,35]. On the other hand, high expression levels

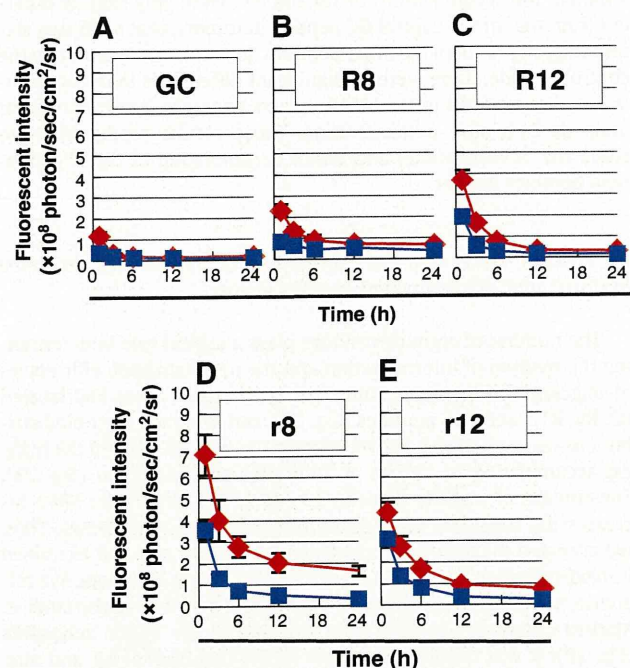


Fig. 3. Time-course study on accumulation of fluorescently labeled oligoarginine peptides in tumor (red) and muscle (blue). Tumor-xenografted mice were injected with each peptide (A, GC; B, R8; C, R12; D, r8; E, r12) (3 nmol each), and then *in vivo* fluorescent imaging of the mice was conducted at 1, 3, 6, 12, and 24 h after injection. Fluorescent intensity in tumor and muscle was analyzed using the IVIS Spectrum system. Data represent the average (\pm SD) of five animals.

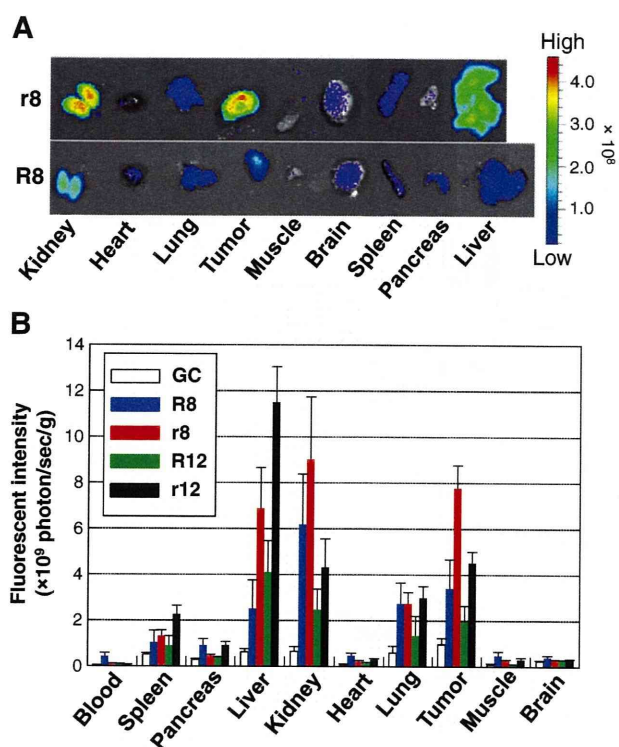


Fig. 4. Biodistribution of fluorescently labeled oligoarginine peptides administrated into tumor-xenografted mice. (A) Fluorescent imaging of each organ and tumor at 24 h after the mice were injected with r8- and R8-alexa660 (3 nmol each), then sacrificed. (B) Fluorescent intensity of tumor and each organ. The mice were sacrificed at 24 h after the injection of alexa660-labeled GC (white), R8 (blue), r8 (red), R12 (green), and r12 (black) peptides (3 nmol each), and then the fluorescent intensity of the tumor and each organ was analyzed using the IVIS Spectrum system. Data represent the average (\pm SD) of five animals.

of proteoglycans have been reported in various cancer cells [36,37], as has the involvement of proteoglycans in various aspects of tumorigenesis, including cell adhesion, growth, and motility [37–39]. Thus, we next examined the importance of membrane-associated proteoglycans in the accumulation of r8-alexa660 in tumor xenografts *in vivo*. Wild-type CHO-K1 cells with membrane-associated proteoglycans, and A-745 cells deficient in GAGs (Fig. 5A), were implanted in the shoulders of nude mice. At 24 h after peptide administration (3 nmol), the fluorescence intensity of r8-alexa660 was higher in the CHO-K1 xenograft than in the A-745 xenograft (Fig. 5B, C), whereas that of alexa660-labeled albumin was almost the same in both xenografts (Supplementary Content Fig. S3). These results suggest that GAGs on plasma membranes may play an important role in the accumulation of r8 peptide in tumors.

3.6. Anticancer effect of r8-conjugated doxorubicin

Doxorubicin is widely used as a therapeutic anticancer agent [40–42]. However, the side effects of the drug, especially cardiotoxicity, are a major drawback [42–44]. To investigate the effects of the r8 peptide on the delivery of doxorubicin to a tumor, we prepared a conjugate of r8 and doxorubicin (r8-doxorubicin). A cross-link was formed between a cysteine introduced at the C-terminus of r8 and the 13-keto position of doxorubicin using maleimidopropionic acid hydrazide as a cross-linker, as reported by Furgeson et al. [29] (Fig. 6A). The hydrazone formed between doxorubicin and the cross-linker cleaves gradually at acidic pH and liberates doxorubicin [29,45,46]. We examined the anticancer activity of the conjugate by comparing it with free doxorubicin *in vitro* (Fig. 6B). Neither the r8-conjugate nor free doxorubicin showed

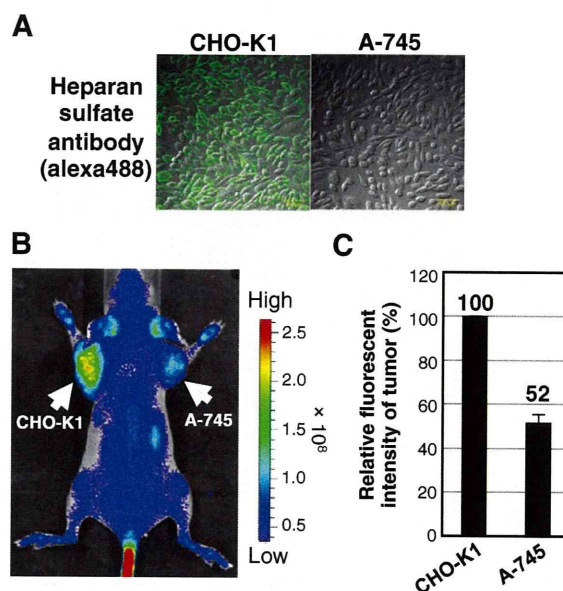


Fig. 5. Importance of glycosaminoglycans on the accumulation of r8 peptide in tumor. (A) Expression of heparan sulfate proteoglycans on cell surface of CHO-K1 and A-745 cells. The cells were stained with anti-heparan sulfate antibody labeled with alexa488. (B) *In vivo* fluorescent imaging of CHO-K1- and A-745-xenografted mice at 24 h after intravenous injection of r8-alexa660 (3 nmol). Arrows show tumor xenografts of CHO-K1 and A-745. (C) Relative fluorescent intensity of tumor xenografts of CHO-K1 and A-745 was analyzed using IVIS Spectrum system under the same conditions in B. Data represent the average (\pm SD) of three animals.

significant suppression of tumor growth at 5 μ M. However, higher cytotoxicity was seen with r8-doxorubicin than with doxorubicin itself when the cells were treated with 10 μ M for 24 h at 37 $^{\circ}$ C, suggesting that the r8-conjugate did not hamper the anticancer activity of doxorubicin, but may have actually enhanced its activity (Fig. 6B). In addition, co-treatment with doxorubicin and the r8 peptide showed no significant effect on cytotoxicity (Fig. 6B).

The conjugate was then analyzed in an *in vivo* assay, based on tumor growth inhibition (Fig. 6C). Tumor-xenografted mice were injected with doxorubicin (4 or 6 mg/kg) or r8-doxorubicin (2 or 4 mg doxorubicin/kg) three times at 24 h intervals. Tumor volumes were measured before (day 0) and after administration, up to 21 days. The administration of 6 mg/kg doxorubicin resulted in a ~50% drop in tumor proliferation during the test period (Fig. 6C), but also a ~20% loss in body weight, suggesting high toxicity (Fig. 6D). No significant decrease in tumor growth was observed at the lower concentration of doxorubicin (4 mg/kg; Fig. 6C). Use of 4 mg doxorubicin/kg r8-doxorubicin led to similar inhibition to that of doxorubicin at 6 mg/kg (Fig. 6C), and no significant decrease in body weight (Fig. 6D). This suggests that conjugation of doxorubicin with r8 may maintain the required anticancer activity while reducing the side effects.

We additionally examined conjugates using an oligoarginine with lower internalization efficiencies. The D-form of the hexaarginine (r6) was used as a carrier peptide. Interestingly, although r6-alexa660 showed comparable tumor accumulation to that of r8-alexa660, the anti-tumor activity of r6-doxorubicin was not as high as that of the r8-conjugate (Supplementary Content Fig. S4).

4. Discussion

Several reports have suggested that arginine-rich CPPs and their conjugates tend to accumulate in certain organs, including the liver, kidney, lung, and spleen. However, few reports have studied the biodistribution of CPPs in tumor-xenografted mice. In the present study, using typical arginine-rich CPPs, we determined that there is a

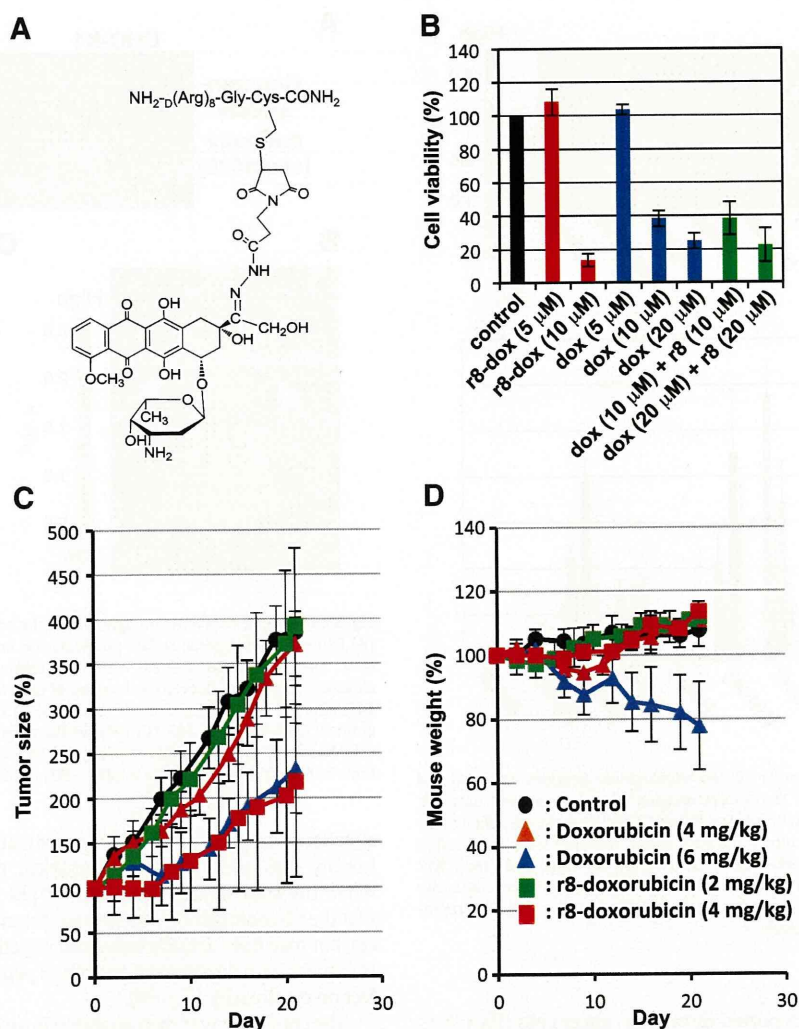


Fig. 6. Anticancer activity of the r8-doxorubicin conjugate. (A) Structure of the r8-doxorubicin conjugate. (B) Cytotoxicity of r8-doxorubicin (r8-dox) and doxorubicin (dox) *in vitro* assay. HeLa cells were treated with each test compound for 24 h at 37 °C, and then the MTT assay was conducted. (C, D) Tumor size (C) and body weight (D) of tumor-bearing mice treated with doxorubicin (4 mg/kg, orange; 6 mg/kg, blue), r8-doxorubicin (2 mg doxorubicin/kg, green; 4 mg doxorubicin/kg, red), and PBS (control, black). Data represent the average (\pm SD) of three (B) and five (C, D) experiments.

considerable difference among peptides regarding their accumulation in tumors: Tat, Pen, and R8 showed a similar degree of accumulation in the kidney, liver, and lung. However, R8 showed higher accumulation in tumor xenografts. A comparison of oligoarginines composed of different numbers of arginines (R2, R8, R12, and R16) revealed that R8 accumulated the most in tumors, followed by R12. D-substitution of the amino acids of R8 and R12 increased accumulation further, where the level of r8 was almost nine-fold higher than that of the control GC peptide. A salient feature of r8 regarding its accumulation in tumors could be its prolonged retention in those tumors. It decreased by 6 h after injection, but this decrease quickly slowed and almost 70% of the level at 6 h remained at 24 h. This level of retention was significantly higher than that exhibited by the other oligoarginine peptides. At the same time, the accumulation levels of r8 in other organs were almost the same as those of the other oligoarginine peptides (slightly higher in the liver and kidney). These results indicate that r8 tends to accumulate more in tumors than do the other arginine-rich CPPs tested.

The detailed mechanism behind this tendency is currently unknown. However, assuming that arginine-rich CPPs composed of D-amino acids may be less susceptible to proteolysis than their L-isomers and that certain numbers of arginine residues are needed to

efficiently interact with tumor cells, the prolonged retention of the D-isomer peptide structures may favor their accumulation in tumors. The higher retention of r8 peptide than R8 in the blood in the early phase after injection may further support this. Interestingly, r12 showed less marked accumulation in tumors than did r8. Compared to r8, r12 may interact more strongly with other organs, including the liver and lung, before arriving at a tumor. Retention of r12 in these organs may result in less accumulation in the tumor. On the other hand, to improve the pharmacokinetic profiles of doxorubicin and other anticancer agents, various formulations have already been reported that provide active [47,48] and passive tumor targeting using the enhanced permeation and retention (EPR) effect [48–50]. Accumulation of serum proteins in solid tumors has also been attributed to the EPR effect [48–50]. Oligoarginine peptides can thus be delivered into tumor tissues by binding to serum proteins. Leakage of the complexes through blood vessels into cancer tissues should result in the transfer of these peptides from serum proteins to tumor-related molecules having higher affinities for these peptides (e.g., proteoglycans), and a certain proportion of oligoarginines would then be trapped by the cancer cells. That r8 showed the highest accumulation in tumor tissues may be explained in terms of its stability in blood and affinity for serum proteins and tumor tissues. L-forms of

oligoarginines are more susceptible to proteolytic enzymes than D-peptides. Degradation of the peptides results in decreased binding affinity for serum proteins as well as less accumulation in tumor tissues. Although r12 was more efficiently taken up by the cells than r8, this peptide also has a higher affinity for serum proteins [51]. This leads to strong retention of r12 by serum proteins when delivered into tumor tissues, whereas r8 fractionated into tumor tissues more readily.

We also found significant *in vivo* accumulation of r8 in wild-type CHO-K1 xenografts but not in GAG-deficient A-745 xenografts. Consistent with the superior *in vitro* cellular uptake of arginine-rich CPPs by CHO-K1 cells versus A-745 cells, the serum-bound r8 should be transferred more favorably to the former xenografts. High expression of proteoglycans in various tumor cells has already been reported [36,37], and the involvement of GAGs in tumor development, including angiogenesis and metastasis, has been suggested [37–39]. Thus, the interaction of r8 with tumor-associated GAGs may promote its accumulation in tumors. In addition, there was no significant difference in accumulation of alexa660-labeled albumin in CHO-K1 and A-745 cells, suggesting that an EPR effect cannot solely explain the accumulation of r8 in tumors and that fractionation of oligoarginines from serum to tumor tissues may be another important factor.

The potential of r8 to deliver an anticancer agent was also assessed using doxorubicin as a model compound (Fig. 6). Doxorubicin is an anthracycline antibiotic that is widely used as an anticancer agent [40–42]. However, the systemic administration of doxorubicin can lead to severe cardiac toxicity [42–44]. In this study, we prepared a conjugate of doxorubicin with r8 and examined the feasibility of the r8-conjugate for tumor treatment. Free doxorubicin can permeate plasma membranes by itself and often shows higher anti-tumor activity than when it is conjugated with carrier molecules. However, in this study, free doxorubicin and r8-doxorubicin exhibited similar anti-tumor activities. This could be because r8 has high membrane permeability and high affinity for cellular DNA and RNA; binding of r8 to cellular nucleic acids may increase the affinity of doxorubicin for its target in the cells and enhance bioactivity.

While 6 mg/kg doxorubicin effectively suppressed tumor growth in mice, this was accompanied by significant weight loss, suggesting strong side effects of doxorubicin. On the other hand, administration of r8-doxorubicin (4 mg doxorubicin/kg) resulted in suppression of tumor proliferation to the same extent as doxorubicin (6 mg/kg), but without causing significant weight loss. Thus, conjugation with r8 may enhance the activity of anticancer agents, making it possible to use lower doses of agents and thereby reduce the side effects. Although r6-alexa660 and r8-alexa660 showed similar degrees of accumulation in tumors, r6-doxorubicin showed less anti-tumor proliferation activity than did r8-doxorubicin. This may be because r6 has a lower affinity for serum proteins and therefore is more easily liberated from serum proteins, whereas its affinity to the acceptors (e.g., tumor-tissue-associated GAGs) is also lower than that of r8. Thus, the retention of r6 in tumor tissues may be almost the same as that of r8. On the other hand, the internalization efficiency of r6 in tumor cells appears to be lower than that of r8, and this may eventually result in the lower anti-tumor activity of r6-doxorubicin than that of the r8-conjugate. Thus, the anti-tumor activity of r8-doxorubicin should be analyzed in terms of a balance between serum binding, affinity for tumor tissue, and internalization efficiency.

In conclusion, our study demonstrates that D-form octaarginine (r8) accumulates in high levels in tumor tissues. Our study was intended to obtain basic information about the *in vivo* distribution of oligoarginine peptides in tumor-xenografted mice. Further studies are needed to assess the utility of using r8 to target different types of cancer cells as well as the feasibility of the simple conjugation of r8 for practical cancer therapy. Such information could lead to more

effective and sophisticated delivery systems for anticancer therapies. The present results may provide a novel starting point for the design of tumor-targeting therapeutic and diagnostic systems.

Acknowledgement

We are grateful for skillful assistance in experiments using NMR spectroscopy by Tomoyuki Yoshimura. This work was supported in part by Grants-in-Aid for Scientific Research from the Ministry of Education, Culture, Sports, Science and Technology of Japan and the Ministry of Health Labour and Welfare of Japan.

Appendix A. Supplementary data

Supplementary data to this article can be found online at doi:10.1016/j.jconrel.2012.01.016.

References

- [1] E. Ruoslahti, M.D. Pierschbacher, New perspectives in cell adhesion: RGD and integrins, *Science* 238 (1987) 491–497.
- [2] S. Liu, Radiolabeled cyclic RGD peptides as integrin alpha(v)beta(3)-targeted radiotracers: maximizing binding affinity via bivalency, *Bioconjug. Chem.* 20 (2009) 2199–2213.
- [3] A.V. Schally, A. Nagy, New approaches to treatment of various cancers based on cytotoxic analogs of LHRH, somatostatin and bombesin, *Life Sci.* 72 (2003) 2305–2320.
- [4] S.M. Okarvi, Peptide-based radiopharmaceuticals and cytotoxic conjugates: potential tools against cancer, *Cancer Treat. Rev.* 34 (2008) 13–26.
- [5] S.E. Pool, E.P. Krenning, G.A. Koning, C.H. van Eijck, J.J. Teunissen, B. Kam, R. Valkema, D.J. Kwekkeboom, M. de Jong, Preclinical and clinical studies of peptide receptor radionuclide therapy, *Semin. Nucl. Med.* 40 (2010) 209–218.
- [6] X.L. Wang, R. Xu, Z.R. Lu, A peptide-targeted delivery system with pH-sensitive amphiphilic cell membrane disruption for efficient receptor-mediated siRNA delivery, *J. Control. Release* 134 (2009) 207–213.
- [7] J. Enbäck, P. Laakkonen, Tumour-homing peptides: tools for targeting, imaging and destruction, *Biochem. Soc. Trans.* 35 (2007) 780–783.
- [8] A. Rivinoja, P. Laakkonen, Identification of homing peptides using the *in vivo* phage display technology, *Meth. Mol. Biol.* 683 (2011) 401–415.
- [9] W. Tai, R. Mahato, K. Cheng, The role of HER2 in cancer therapy and targeted drug delivery, *J. Control. Release* 146 (2010) 264–275.
- [10] V. Askoxylakis, S. Zitzmann-Kolbe, F. Zoller, A. Altmann, A. Markert, S. Rana, A. Marr, W. Mier, J. Debus, U. Haberkorn, Challenges in optimizing a prostate carcinoma binding peptide, identified through the phage display technology, *Molecules* 16 (2011) 1559–1578.
- [11] E. Vivès, P. Brodin, B. Lebleu, A truncated HIV-1 Tat protein basic domain rapidly translocates through the plasma membrane and accumulates in the cell nucleus, *J. Biol. Chem.* 272 (1997) 16010–16017.
- [12] J.B. Rothbard, S. Garlington, Q. Lin, T. Kirschberg, E. Kreider, P.L. McGrane, P.A. Wender, P.A. Khavari, Conjugation of arginine oligomers to cyclosporin A facilitates topical delivery and inhibition of inflammation, *Nat. Med.* 6 (2000) 1253–1257.
- [13] S. Futaki, T. Suzuki, W. Ohashi, T. Yagami, S. Tanaka, K. Ueda, Y. Sugiura, Arginine-rich peptides. An abundant source of membrane-permeable peptides having potential as carriers for intracellular protein delivery, *J. Biol. Chem.* 276 (2001) 5836–5840.
- [14] Special Theme Issue on Membrane Permeable Peptide Vectors: Chemistry and Functional Design for the Therapeutic Applications, S. Futaki (Ed.), *Adv. Drug Deliv. Rev.*, vol. 60, 2008, pp. 447–614.
- [15] E.A. Dubikovskaya, S.H. Thorne, T.H. Pillow, C.H. Contag, P.A. Wender, Overcoming multidrug resistance of small-molecule therapeutics through conjugation with releasable octaarginine transporters, *Proc. Natl. Acad. Sci. U. S. A.* 105 (2008) 12128–12133.
- [16] S. Fawell, J. Seery, Y. Daikh, C. Moore, L.L. Chen, B. Pepinsky, J. Barsoum, Tat-mediated delivery of heterologous proteins into cells, *Proc. Natl. Acad. Sci. U. S. A.* 91 (1994) 664–668.
- [17] S.R. Schwarze, A. Ho, A. Vocero-Akbani, S.F. Dowdy, *In vivo* protein transduction: delivery of a biologically active protein into the mouse, *Science* 285 (1999) 1569–1572.
- [18] H.J. Lee, W.M. Pardridge, Pharmacokinetics and delivery of tat and tat-protein conjugates to tissues *in vivo*, *Bioconjug. Chem.* 12 (2001) 995–999.
- [19] K.E. Bullok, M. Dyszlewski, J.L. Prior, C.M. Pica, V. Sharma, D. Piwnicka-Worms, Characterization of novel histidine-tagged Tat-peptide complexes dual-labeled with (99m)Tc-tricarbonyl and fluorescein for scintigraphy and fluorescence microscopy, *Bioconjug. Chem.* 13 (2002) 1226–1237.
- [20] P. Wunderbaldinger, L. Josephson, R. Weissleder, Tat peptide directs enhanced clearance and hepatic permeability of magnetic nanoparticles, *Bioconjug. Chem.* 13 (2002) 264–268.
- [21] S. Kameyama, R. Okada, T. Kikuchi, T. Omura, I. Nakase, T. Takeuchi, Y. Sugiura, S. Futaki, Distribution of immunoglobulin Fab fragment conjugated with HIV-1 REV

- peptide following intravenous administration in rats, *Mol. Pharm.* 3 (2006) 174–180.
- [22] S. Kameyama, M. Horie, T. Kikuchi, T. Omura, T. Takeuchi, I. Nakase, Y. Sugiura, S. Futaki, Effects of cell-permeating peptide binding on the distribution of 125I-labeled Fab fragment in rats, *Bioconjug. Chem.* 17 (2006) 597–602.
- [23] E.L. Snyder, B.R. Meade, C.C. Saenz, S.F. Dowdy, Treatment of terminal peritoneal carcinomatosis by a transducible p53-activating peptide, *PLoS Biol.* 2 (2004) E36.
- [24] M. Tan, K.H. Lan, J. Yao, C.H. Lu, M. Sun, C.L. Neal, J. Lu, D. Yu, Selective inhibition of ErbB2-overexpressing breast cancer in vivo by a novel TAT-based ErbB2-targeting signal transducers and activators of transcription 3-blocking peptide, *Cancer Res.* 66 (2006) 3764–3772.
- [25] S. Kizaka-Kondoh, S. Itasaka, L. Zeng, S. Tanaka, T. Zhao, Y. Takahashi, K. Shibuya, K. Hirota, G.L. Semenza, M. Hiraoka, Selective killing of hypoxia-inducible factor-1-active cells improves survival in a mouse model of invasive and metastatic pancreatic cancer, *Clin. Cancer Res.* 15 (2009) 3433–3441.
- [26] E.S. Olson, T. Jiang, T.A. Aguilera, Q.T. Nguyen, L.G. Ellies, M. Scadeng, R.Y. Tsien, Activatable cell penetrating peptides linked to nanoparticles as dual probes for in vivo fluorescence and MR imaging of proteases, *Proc. Natl. Acad. Sci. U. S. A.* 107 (2010) 4311–4316.
- [27] S. Futaki, M. Niwa, I. Nakase, A. Tadokoro, Y. Zhang, M. Nagaoka, N. Wakako, Y. Sugiura, Arginine carrier peptide bearing Ni(II) chelator to promote cellular uptake of histidine-tagged proteins, *Bioconjug. Chem.* 15 (2004) 475–481.
- [28] R.P. Haugland, *Handbook of Fluorescent Probes and Research Products*, ninth edition Molecular Probes Inc, 2002.
- [29] D.Y. Furgeson, M.R. Dreher, A. Chilkoti, Structural optimization of a “smart” doxorubicin-polypeptide conjugate for thermally targeted delivery to solid tumors, *J. Control. Release* 110 (2006) 362–369.
- [30] K. Sano, T. Temma, T. Azuma, R. Nakai, M. Narazaki, Y. Kuge, H. Saji, A Pre-targeting Strategy for MR Imaging of Functional Molecules Using Dendritic Gd-Based Contrast Agents, *Mol. Imaging Biol.* 13 (2011) 1196–1203.
- [31] I. Nakase, M. Niwa, T. Takeuchi, K. Sonomura, N. Kawabata, Y. Koike, M. Takehashi, S. Tanaka, K. Ueda, J.C. Simpson, A.T. Jones, Y. Sugiura, S. Futaki, Cellular uptake of arginine-rich peptides: roles for macropinocytosis and actin rearrangement, *Mol. Ther.* 10 (2004) 1011–1022.
- [32] D. Derossi, A.H. Joliot, G. Chassaing, A. Prochiantz, The third helix of the Antennapedia homeodomain translocates through biological membranes, *J. Biol. Chem.* 269 (1994) 10444–10450.
- [33] R. Bessalle, A. Kapitkovsky, A. Gorea, I. Shalit, M. Fridkin, All-D-magainin: chirality, antimicrobial activity and proteolytic resistance, *FEBS Lett.* 274 (1990) 151–155.
- [34] I. Nakase, A. Tadokoro, N. Kawabata, T. Takeuchi, H. Katoh, K. Hiramoto, M. Negishi, M. Nomizu, Y. Sugiura, S. Futaki, Interaction of arginine-rich peptides with membrane-associated proteoglycans is crucial for induction of actin organization and macropinocytosis, *Biochemistry* 46 (2007) 492–501.
- [35] I. Nakase, H. Hirose, G. Tanaka, A. Tadokoro, S. Kobayashi, T. Takeuchi, S. Futaki, Cell-surface accumulation of flock house virus-derived peptide leads to efficient internalization via macropinocytosis, *Mol. Ther.* 17 (2009) 1868–1876.
- [36] K. Matsuda, H. Maruyama, F. Guo, J. Kleeff, J. Itakura, Y. Matsumoto, A.D. Lander, M. Korc, Glypican-1 is overexpressed in human breast cancer and modulates the mitogenic effects of multiple heparin-binding growth factors in breast cancer cells, *Cancer Res.* 61 (2001) 5562–5569.
- [37] J.H. Lee, H. Park, H. Chung, S. Choi, Y. Kim, H. Yoo, T.Y. Kim, H.J. Hann, I. Seong, J. Kim, K.G. Kang, I.O. Han, E.S. Oh, Syndecan-2 regulates the migratory potential of melanoma cells, *J. Biol. Chem.* 284 (2009) 27167–27175.
- [38] R.D. Sanderson, Heparan sulfate proteoglycans in invasion and metastasis, *Semin. Cell Dev. Biol.* 12 (2001) 89–98.
- [39] I. Vlodevsky, O. Goldshmidt, E. Zcharia, R. Atzmon, Z. Rangini-Guatta, M. Elkin, T. Peretz, Y. Friedmann, Mammalian heparanase: involvement in cancer metastasis, angiogenesis and normal development, *Semin. Cancer Biol.* 12 (2002) 121–129.
- [40] R.L. Momparler, M. Karon, S.E. Siegel, F. Avila, Effect of adriamycin on DNA, RNA, and protein synthesis in cell-free systems and intact cells, *Cancer Res.* 36 (1976) 2891–2895.
- [41] C.A. Frederick, L.D. Williams, G. Ughetto, G.A. van der Marel, J.H. van Boom, A. Rich, A.H. Wang, Structural comparison of anticancer drug-DNA complexes: adriamycin and daunomycin, *Biochemistry* 29 (1990) 2538–2549.
- [42] D.A. Gewirtz, A critical evaluation of the mechanisms of action proposed for the antitumor effects of the anthracycline antibiotics adriamycin and daunorubicin, *Biochem. Pharmacol.* 57 (1999) 727–741.
- [43] M.J. Aiken, V. Suhag, C.A. Garcia, E. Acio, S. Moreau, D.A. Priebat, S.P. Chennupati, D. Van Nostrand, Doxorubicin-induced cardiac toxicity and cardiac rest gated blood pool imaging, *Clin. Nucl. Med.* 34 (2009) 762–767.
- [44] Y.W. Zhang, J. Shi, Y.J. Li, L. Wei, Cardiomyocyte death in doxorubicin-induced cardiotoxicity, *Arch. Immunol. Ther. Exp. (Warsz.)* 57 (2009) 435–445.
- [45] T. Kaneko, D. Willner, I. Monoković, J.O. Knipe, G.R. Braslawsky, R.S. Greenfield, D.M. Vyas, New hydrazone derivatives of adriamycin and their immunoconjugates—a correlation between acid stability and cytotoxicity, *Bioconjug. Chem.* 2 (1991) 133–141.
- [46] S. Cai, S. Thati, T.R. Bagby, H.M. Diab, N.M. Davies, M.S. Cohen, M.L. Forrest, Localized doxorubicin chemotherapy with a biopolymeric nanocarrier improves survival and reduces toxicity in xenografts of human breast cancer, *J. Control. Release* 146 (2010) 212–218.
- [47] T.M. Allen, Ligand-targeted therapeutics in anticancer therapy, *Nat. Rev. Cancer* 2 (2002) 750–763.
- [48] F. Danhier, O. Feron, V. Préat, To exploit the tumor microenvironment: passive and active tumor targeting of nanocarriers for anti-cancer drug delivery, *J. Control. Release* 148 (2010) 135–146.
- [49] Y. Matsumura, H. Maeda, A new concept for macromolecular therapeutics in cancer chemotherapy: mechanism of tumorotropic accumulation of proteins and the antitumor agent smancs, *Cancer Res.* 46 (1986) 6387–6392.
- [50] H. Maeda, J. Wu, T. Sawa, Y. Matsumura, K. Hori, Tumor vascular permeability and the EPR effect in macromolecular therapeutics: a review, *J. Control. Release* 65 (2000) 271–284.
- [51] M. Kosuge, T. Takeuchi, I. Nakase, A.T. Jones, S. Futaki, Cellular internalization and distribution of arginine-rich peptides as a function of extracellular peptide concentration, serum, and plasma membrane associated proteoglycans, *Bioconjug. Chem.* 19 (2008) 656–664.

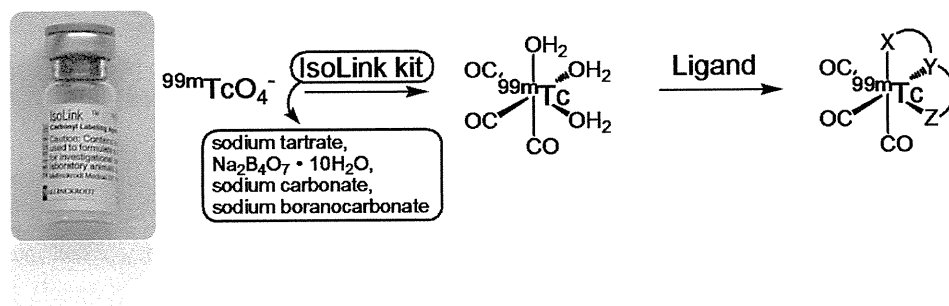
Chart 1. Synthesis of ^{99m}Tc Tricarbonyl Complex (I)

Table 1. Microwave-Assisted Synthesis of Organorhenium Complexes of PAMA

Entry	Solvent	Time (min)	Yield (%) ^{a)}		
			2	3	4
1	MeOH	5	15	18	21
2	H ₂ O	5	96	4	—
3	EtOH	5	5	87	—
4	DMF	5	—	58	—
5	MeCN	5	—	74	—

a) Determined by LC/MS analysis.

$^{99m}\text{Tc}(\text{CO})_3$ complexes is required.

Microwave technology has been successfully applied to enhance radiolabeling reactions.^{4–6)} When microwave is used as a source of energy, the reactions proceed in a short time and in much higher yields than those performed under the conventional thermal conditions.

In the present paper, we report a rapid and facile method of synthesizing $^{99m}\text{Tc}(\text{CO})_3$ complexes using microwave technology in detail.

Results and Discussion

First, we tried to develop a rapid and efficient synthetic method of $^{99m}\text{Tc}(\text{CO})_3$ complexes carrying 2-picolylamine-*N*-acetic acid (PAMA) as a chelating ligand, which is often used in the preparation of various ^{99m}Tc -labeled probes.^{7,8)} In the synthesis of $^{99m}\text{Tc}(\text{CO})_3$ -PAMA complexes, PAMA has been incorporated as an ester form in a reaction with a bioactive ligand, followed by hydrolysis of the resulting intermediate, and subsequent formation of a chelate with the metal ion by heating. However, it was pointed out that decomposition of the bioactive ligand during the hydrolysis and the long reaction process decrease the chemical yield and reproducibility. Thus, use of a microwave reaction was scrutinized to achieve direct formation of $^{99m}\text{Tc}(\text{CO})_3$ -PAMA complex from $[\text{}^{99m}\text{Tc}(\text{CO})_3(\text{H}_2\text{O})_3]^+$ and PAMAE since ethyl esters could generally be cleaved under extreme conditions in the presence of a small amount of salts by the mechanisms of hydrolysis or elimination of ethylene.⁹⁾ In advance of the one-step synthesis of $^{99m}\text{Tc}(\text{CO})_3$ -PAMA complex, Re was used instead of Tc

because of the similarity of coordination structure, *i.e.*, a bipyramidal form, and the absence of stable isotopes for Tc.

To optimize the reaction condition of conversion from **1** to **2**, we performed the reaction in several solvents such as water, MeOH, EtOH, MeCN, and *N,N*-dimethylformamide (DMF) (Table 1). We fixed the condition for microwave application as follows: temperature: 110°C, pressure: 17 bar, and power: 300 W. As a result, the reaction in water gave **2** in an excellent yield (96%, Table 1, entry 2), while the reaction in polar aprotic solvents such as DMF and MeCN gave **3** as a sole product (Table 1, entries 3–5). Thus, MeOH and water were chosen as the solvents for further optimizations.

Next, we compared the reaction using microwaves for heating with that using an oil bath. Using MeOH as a solvent, **2** was obtained in a yield of 59% under conventional heating for 180 min condition and 64% under microwave heating for 90 min (Table 2). The reaction with microwave heating proceeded more rapidly than that with conventional heating, and the reactions in a shorter time yielded **3** and **4**, preferentially (Table 2, entries 1, 2, 4, 5). This result meant that intermediates **3** and **4** were initially generated and subsequent hydrolysis afforded **2**.

Meanwhile, when water was used as a solvent, **2** was obtained at 84% under conventional heating for 90 min and 94% under microwave heating for 30 s (Table 3). Namely, the yield of **2** was increased and that of **3** was decreased under the condition of microwave heating.

Next, we investigated the effect of MeOH as a co-solvent on microwave-assisted synthesis of $\text{Re}(\text{CO})_3$ -PAMA, taking

Table 2. Synthesis of $\text{Re}(\text{CO})_3$ -PAMA in MeOH: Comparison between Microwave Heating and Conventional Heating

Entry	Heating method	Time (min)	Yield (%) ^{a)}		
			2	3	4
1	Oil bath	90	20	47	13
2		120	21	28	4
3		180	59	13	1
4	Microwave	10	18	32	13
5		30	40	14	8
6		60	53	12	5
7		90	64	12	2

^{a)} Determined by LC/MS analysis.

Table 3. Synthesis of $\text{Re}(\text{CO})_3$ -PAMA in H_2O : Comparison between Microwave Heating and Conventional Heating

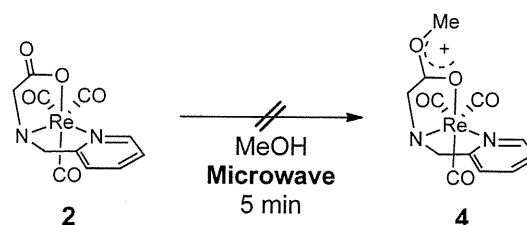
Entry	Heating method	Time (min)	Yield (%) ^{a)}	
			2	3
1	Oil bath	5	64	22
2		60	72	12
3		90	84	10
4	Microwave	30 s	94	4
5		1	95	5
6		5	96	4

^{a)} Determined by LC/MS analysis.

into account the solubility of organic compounds in water (Table 4). There was no significant decrease in the yield of **2** until the ratio of MeOH in the solvent reached 50% (Table 4, entries 2, 3); however, decrease in the yield of **2** and increase in the yield of **4** were observed (Table 4, entries 4, 5). This result suggested the possibility of providing $\text{Re}(\text{CO})_3$ -PAMA complexes in sufficient yield under microwave heating condition using a solvent containing less than 50% MeOH.

This result encouraged us to investigate the mechanism of the reaction. The reaction was scrutinized using solvents containing MeOH and water at several ratios under the condition of microwave heating. Compound **4** was not obtained from **2** in MeOH (Chart 2), while compounds **2** and **4** were obtained from **3** (Chart 3).

Thus, the reaction seemed to proceed *via* the following pathway (Fig. 2). First, the intermediate **A** could be generated by the reaction of $[\text{Re}(\text{CO})_3(\text{H}_2\text{O})_3]\text{Br}$ with PAMAEE. Next, **A** could be converted to **3** owing to the Lewis acidity of the rhenium cation. Finally, compound **3** could be transformed to **2** *via* labile intermediate **3'**. When MeOH was used as a solvent,

Chart 2. Microwave-Assisted Reaction of $\text{Re}(\text{CO})_3$ -PAMA-OMe from $\text{Re}(\text{CO})_3$ -PAMA in MeOH

ester exchange from **3** to **4** would proceed *facilely*. However, finally, **2** was generated from both intermediate **3** and **4**. Microwave irradiation seemed to accelerate the reactions from **3** to **3'** and from **3** to **4**.

Next, we applied the reaction to synthesize $^{99\text{m}}\text{Tc}(\text{CO})_3$ -PAMA complex. When water was used as a solvent under the condition of microwave heating, the radiochemical yield of $^{99\text{m}}\text{Tc}(\text{CO})_3$ -PAMA complex was over 99% (Table 5, entry

Table 4. Effect of MeOH as a Co-solvent on Microwave-Assisted Synthesis of $\text{Re}(\text{CO})_3$ -PAMA

Entry	Solvent	Yield (%) ^{a)}		
		2	3	4
1	H ₂ O	96	4	—
2	H ₂ O:MeOH = 3:1	85	4	—
3	H ₂ O:MeOH = 1:1	85	4	—
4	H ₂ O:MeOH = 1:3	76	5	4
5	H ₂ O:MeOH = 1:9	56	13	9
6	MeOH	15	18	21

a) Determined by LC/MS analysis.

Table 5. Effect of MeOH as a Co-solvent on Microwave-Assisted Synthesis of $^{99\text{m}}\text{Tc}(\text{CO})_3$ -PAMA

Entry	Solvent	Time (min)	Radiochemical yield (%)
			2
1	H ₂ O	10 s	>99
2	H ₂ O	1	>99
3	H ₂ O:MeOH = 1:1	1	>99
4	H ₂ O:MeOH = 1:3	1	62
5	H ₂ O:MeOH = 1:9	1	63

1). We investigated the effect of MeOH as a co-solvent on microwave-assisted synthesis of $^{99\text{m}}\text{Tc}(\text{CO})_3$ -PAMA complex. There was no significant decrease in the yield while the content ratios of MeOH were lower than 50%; however, the yield of $^{99\text{m}}\text{Tc}(\text{CO})_3$ -PAMA decreased as the ratio of MeOH became higher (Table 5, entries 3—5).

Conclusion

In the present study, we could improve the reaction of PAMAEE and $[^{99\text{m}}\text{Tc}(\text{CO})_3(\text{H}_2\text{O})_3]^+$ using microwaves. Since no stable isotopes exist for Tc, the usefulness of microwaves was firstly examined using Re, which is an element in the same group of the periodic table as Tc, and which also forms bipyramidal complexes.

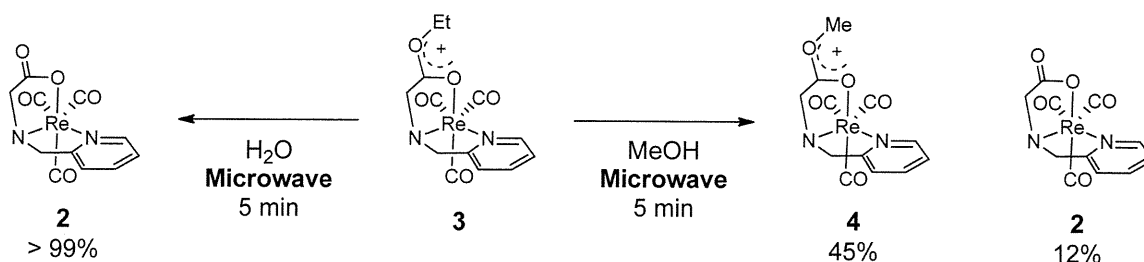
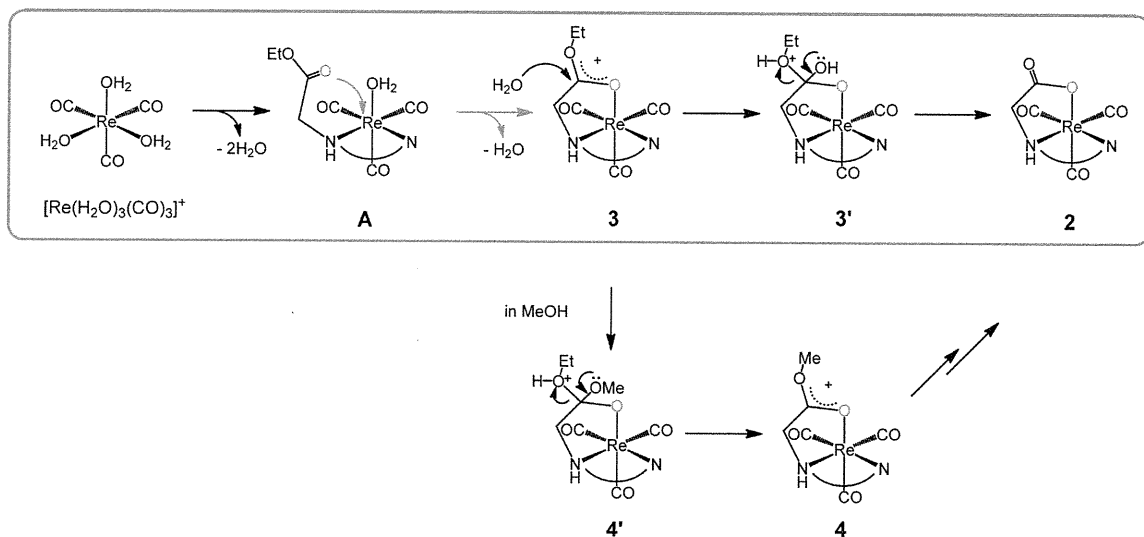
When water was used as the reaction solvent in the synthesis of the Re complexes using PAMAEE as the ligand, the desired complex $\text{Re}(\text{CO})_3$ -PAMA could be synthesized at a high yield (94%) without requiring hydrolysis of the ethyl ester by irradiating microwaves for 30 s. However, it should be considered that the reaction substrates would not dissolve and the reaction would not proceed in the case where a hydrophobic molecule is bound to a ligand as a bioactive compound. Thus, mixed solvents of water and MeOH were tested to investigate the effects of the ratios of the solvents. As a result, the reac-

tivity was not greatly affected until the proportion of MeOH reached 50%, when the microwaves were irradiated for less than 5 min.

The reaction mechanism accelerated by microwaves was considered on the basis of the above results. First, PAMAEE reacted with $[\text{Re}(\text{CO})_3(\text{H}_2\text{O})_3]\text{Br}$ to form $\text{Re}(\text{CO})_3$ -PAMA-OEt by treating the rhenium cation as a Lewis acid. Subsequent hydrolysis of the intermediate proceeded to afford the target complex, $\text{Re}(\text{CO})_3$ -PAMA. The results also suggested that the hydrolysis of the intermediate $\text{Re}(\text{CO})_3$ -PAMA-OEt was accelerated by microwaves.

On the basis of the results obtained with the Re complex, synthesis of $^{99\text{m}}\text{Tc}$ complex was carried out. The target complex could be synthesized in high yield by irradiating microwaves within 10 s and using water as the solvent. The yield of the reaction depended on the ratio of water and MeOH, similarity to the synthesis of Re complex. After scrutinizing the conditions, it was found that the reaction within 1 min of irradiation of microwaves was not greatly affected while the MeOH content was less than 50%.

The above results demonstrated that microwaves were useful for rapid and simple synthesis of $^{99\text{m}}\text{Tc}(\text{CO})_3$ complexes.

Chart 3. Microwave-Assisted Reaction of $\text{Re}(\text{CO})_3\text{-PAMA-OEt}$ in MeOH or WaterFig. 2. Plausible Mechanism of Microwave-Assisted Synthesis of $\text{Re}(\text{CO})_3\text{-PAMA}$

Experimental

^1H - and ^{13}C -NMR spectra were obtained on a JNM-AL400 spectrometer (JEOL) or JNM-LA500 (JEOL) with $\text{DMSO-}d_6$ as a solvent and tetramethylsilane as an internal standard. Melting points are uncorrected and were measured on a SRS OptiMelt MPA100 melting point apparatus. Liquid chromatography-mass spectrometry was performed using a Shimadzu MS-2010 MS detector and SPD-10AP UV detector with a LC-10AP solvent delivery system and C-18 AR-II column ($4.6 \times 150 \text{ mm}$) at a flow rate of 1.0 mL/min and monitoring at 245 nm . Analytical HPLC was performed using an Aloka NDW-351D detector with a Shimadzu LC-20A solvent delivery system and C-18 AR-II column ($4.6 \times 150 \text{ mm}$) at a flow rate of 1.0 mL/min . The elution protocols used were as follows: Solvent A=MeCN, Solvent B=water, Gradient elution 20—55% A. Mass spectra (MS) were determined on a JMS-HX/HX110 A model (JEOL). Microwave reactions were performed using a CEM Discover. Infrared spectra were obtained on a Shimadzu IRPrestige-21 or Shimadzu FTIR-8300. All chemicals used were of reagent grade. The precursor triaquatricarbonylrhenium bromide was synthesized according to a previously published procedure.¹⁰

Synthesis of $\text{Re}(\text{CO})_3\text{-PAMA}$ Complexes. Experiment of Table 1 Method 1: Triaquatricarbonylrhenium bromide (32.7 mg , $80.8 \mu\text{mol}$) was added to a MeOH solution (1.0 mL) of **1** (15.7 mg , $80.8 \mu\text{mol}$) in a microwave vial (5.0 mL). The reaction vial was crimp-sealed prior to heating in the microwave at 110°C , 17 bar (max), and 300 W (max) for 5 min with

stirring. The reaction mixture was chilled, and then analyzed by LC-MS atmospheric pressure chemical ionization (APCI). **2** (15%), **3** (18%), **4** (21%).

Method 2: Triaquatricarbonylrhenium bromide (34.3 mg , $85.0 \mu\text{mol}$) was added to an aqueous solution (1.0 mL) of **1** (16.5 mg , $85.0 \mu\text{mol}$) in a microwave vial (5.0 mL). The reaction vial was crimp-sealed prior to heating in the microwave at 110°C , 17 bar (max), and 300 W (max) for 5 min with stirring. The reaction mixture was chilled, and then analyzed by LC-MS (APCI). **2** (96%), **3** (4%).

Method 3: Triaquatricarbonylrhenium bromide (16.5 mg , $40.9 \mu\text{mol}$) was added to an EtOH solution (1.0 mL) of **1** (8.0 mg , $40.9 \mu\text{mol}$) in a microwave vial (5.0 mL). The reaction vial was crimp-sealed prior to heating in the microwave at 110°C , 17 bar (max), and 300 W (max) for 5 min with stirring. The reaction mixture was chilled, and then analyzed by LC-MS atmospheric pressure chemical ionization (APCI). **2** (5%), **3** (87%).

Method 4: Triaquatricarbonylrhenium bromide (6.2 mg , $15.4 \mu\text{mol}$) was added to a DMF solution (1.0 mL) of **1** (3.0 mg , $15.4 \mu\text{mol}$) in a microwave vial (5.0 mL). The reaction vial was crimp-sealed prior to heating in the microwave at 110°C , 17 bar (max), and 300 W (max) for 5 min with stirring. The reaction mixture was chilled, and then analyzed by LC-MS (APCI). **3** (58%).

Method 5: Triaquatricarbonylrhenium bromide (13.9 mg , $34.5 \mu\text{mol}$) was added to an MeCN solution (1.0 mL) of **1** (6.7 mg , $34.5 \mu\text{mol}$) in a microwave vial (5.0 mL). The reaction

vial was crimp-sealed prior to heating in the microwave at 110°C, 17 bar (max), and 300 W (max) for 5 min with stirring. The reaction mixture was chilled, and then analyzed by LC-MS (APCI). **3** (74%).

Tricarbonyl (N-(2-Pyridinylmethyl)glycine)rhodium (Re(CO)₃-PAMA; 2) Triaquatricarbonylrhodium bromide (208.1 mg, 514.9 μmol) was added to a H₂O (3.0 mL) and MeOH (0.5 mL) solution (3.0 mL) of **1** (100.0 mg, 514.9 μmol) in a microwave vial (10.0 mL). The reaction vial was crimp-sealed prior to heating in the microwave at 110°C and 300 W (max) for 5 min with stirring. The reaction mixture was chilled, filtrated, and washed with CH₂Cl₂ to give a residue (126.2 mg; 56%) of **2** as a white powder.

White Powder: mp 251–256°C. ¹H-NMR (500 MHz, DMSO-*d*₆) δ: 8.81 (d, *J*=5.5 Hz, 1H), 8.12 (dt, *J*=7.8, 1.1 Hz, 1H), 7.75 (d, *J*=7.8 Hz, 1H), 7.57 (t, *J*=6.6 Hz, 1H), 7.22 (t, *J*=6.2 Hz, 1H), 4.58 (d, *J*=16.7 Hz, 1H), 4.50 (dd, *J*=5.1, 16.6 Hz, 1H), 3.65 (dd, *J*=8.1, 17.3 Hz, 1H), 3.25 (d, *J*=17.3 Hz, 1H). ¹³C-NMR (125 MHz, DMSO-*d*₆) δ: 197.8, 197.5, 197.4, 179.5, 160.0, 152.0, 140.2, 125.4, 123.7, 62.0, 53.9. IR (KBr) cm⁻¹: 3129, 2934, 2361, 2023, 1913, 1888, 1624, 1445, 1381. FAB-MS *m/z*: 437.0153 (Calcd for C₁₁H₁₀N₂O₃Re: 437.0148). MS (FAB) *m/z*: 437 (M⁺+H, 100).

Tricarbonyl (N-(2-Pyridinylmethyl)glycineethylester)rhodium (Re(CO)₃-PAMA-OEt; 3) Triaquatricarbonylrhodium bromide (208.1 mg, 514.9 μmol) was added to an EtOH solution (3.0 mL) of **1** (100.0 mg, 514.9 μmol) in a microwave vial (10.0 mL). The reaction vial was crimp-sealed prior to heating in the microwave at 110°C and 300 W (max) for 5 min with stirring. The reaction mixture was chilled, filtrated, and washed with CH₂Cl₂ to give a residue (153.7 mg; 62%) of **3** as a yellow powder.

Yellow Crystals: mp 179–181°C. ¹H-NMR (500 MHz, DMSO-*d*₆) δ: 8.75 (d, *J*=4.9 Hz, 1H), 8.06 (dt, *J*=7.7, 1.5 Hz, 1H), 7.72 (d, *J*=7.9 Hz, 1H), 7.51 (t, *J*=6.6 Hz, 1H), 5.45 (t, *J*=6.4 Hz, 1H), 4.90 (dd, *J*=16.3, 5.8 Hz, 1H), 4.32 (dd, *J*=16.4, 6.9 Hz, 1H), 4.14–4.25 (m, 2H), 4.05 (dd, *J*=16.5, 5.9 Hz, 1H), 3.90 (dd, *J*=16.4, 6.7 Hz, 1H), 1.24 (t, *J*=7.1 Hz, 3H). ¹³C-NMR (125 MHz, DMSO-*d*₆) δ: 196.7, 196.0, 191.6, 168.6, 160.3, 152.3, 139.6, 125.0, 122.7, 61.0, 58.8, 58.3, 13.9. IR (KBr) cm⁻¹: 3175, 2988, 2941, 2021, 1929, 1871, 1746. FAB-MS *m/z*: 465.0464 (Calcd for C₁₃H₁₄N₂O₃Re: 465.0461). MS (FAB) *m/z*: 465 (M⁺, 100).

Tricarbonyl (N-(2-Pyridinylmethyl)glycinemethylester)rhodium (Re(CO)₃-PAMA-OMe; 4) Triaquatricarbonylrhodium bromide (224.3 mg, 554.9 μmol) was added to a MeOH solution (3.0 mL) of **1** (100.0 mg, 554.9 μmol) in a microwave vial (10.0 mL). The reaction vial was crimp-sealed prior to heating in the microwave at 110°C and 300 W (max) for 5 min with stirring. The reaction mixture was chilled, filtrated, and washed with CH₂Cl₂ to give a residue (173.2 mg; 66%) of **4** as a yellow powder.

Yellow Crystals: mp 221–223°C. ¹H-NMR (400 MHz, DMSO-*d*₆) δ: 8.74 (d, *J*=5.4 Hz, 1H), 8.05 (t, *J*=7.6 Hz, 1H), 7.70 (d, *J*=7.8 Hz, 1H), 7.50 (t, *J*=6.6 Hz, 1H), 5.47 (t, *J*=6.2 Hz, 1H), 4.89 (dd, *J*=16.3, 5.6 Hz, 1H), 4.31 (dd, *J*=16.3, 6.8 Hz, 1H), 4.06 (dd, *J*=16.2, 6.2 Hz, 1H), 3.91 (dd, *J*=16.3, 6.6 Hz, 1H), 3.71 (s, 3H). ¹³C-NMR (100 MHz, DMSO-*d*₆) δ: 196.8, 196.0, 191.7, 169.1, 160.3, 152.3, 139.7, 125.1, 122.8, 58.8, 58.1, 52.0. IR (KBr) cm⁻¹: 3173, 2359, 2021, 1925, 1879, 1751, 1611, 1445. FAB-MS *m/z*: 451.0310 (Calcd for

C₁₃H₁₄N₂O₃Re: 451.0304). MS (FAB) *m/z*: 451 (M⁺, 100).

Experiment of Table 2 Methods 1–3: Triaquatricarbonylrhodium bromide (37.7 mg, 93.2 μmol) was added to a MeOH solution (1.0 mL) of **1** (18.1 mg, 93.2 μmol) in a flask. The reaction mixture was refluxed with stirring. The reaction mixture was chilled, and then analyzed by LC-MS (APCI) for each time.

Entry 1: 90 min, **2** (20%), **3** (47%), **4** (13%).

Entry 2: 120 min, **2** (21%), **3** (28%), **4** (4%).

Entry 3: 180 min, **2** (59%), **3** (13%), **4** (1%).

Method 4: Triaquatricarbonylrhodium bromide (38.5 mg, 95.3 μmol) was added to a MeOH solution (1.0 mL) of **1** (18.5 mg, 95.3 μmol) in a microwave vial (5.0 mL). The reaction vial was crimp-sealed prior to heating in the microwave at 110°C, 17 bar (max), and 300 W (max) for 10 min with stirring. The reaction mixture was chilled, and then analyzed by LC-MS (APCI). **2** (18%), **3** (32%), **4** (13%).

Method 5: Triaquatricarbonylrhodium bromide (35.6 mg, 88.0 μmol) was added to a MeOH solution (1.0 mL) of **1** (17.1 mg, 88.0 μmol) in a microwave vial (5.0 mL). The reaction vial was crimp-sealed prior to heating in the microwave at 110°C, 17 bar (max), and 300 W (max) for 60 min with stirring. The reaction mixture was chilled, and then analyzed by LC-MS (APCI). **2** (40%), **3** (14%), **4** (8%).

Method 6: Triaquatricarbonylrhodium bromide (32.5 mg, 80.3 μmol) was added to a MeOH solution (1.0 mL) of **1** (15.6 mg, 80.3 μmol) in a microwave vial (5.0 mL). The reaction vial was crimp-sealed prior to heating in the microwave at 110°C, 17 bar (max), and 300 W (max) for 10 min with stirring. The reaction mixture was chilled, and then analyzed by LC-MS (APCI). **2** (53%), **3** (12%), **4** (5%).

Method 7: Triaquatricarbonylrhodium bromide (30.4 mg, 75.2 μmol) was added to a MeOH solution (1.0 mL) of **1** (14.6 mg, 75.2 μmol) in a microwave vial (5.0 mL). The reaction vial was crimp-sealed prior to heating in the microwave at 110°C, 17 bar (max), and 300 W (max) for 90 min with stirring. The reaction mixture was chilled, and then analyzed by LC-MS (APCI). **2** (64%), **3** (12%), **4** (2%).

Experiment of Table 3 Methods 1–3: Triaquatricarbonylrhodium bromide (37.7 mg, 93.2 μmol) was added to an aqueous solution (1.0 mL) of **1** (18.1 mg, 93.2 μmol) in a flask. The reaction mixture was refluxed with stirring. The reaction mixture was chilled, and then analyzed by LC-MS (APCI) for each time.

Entry 1: 5 min, **2** (64%), **3** (22%).

Entry 2: 60 min, **2** (72%), **3** (12%).

Entry 3: 90 min, **2** (84%), **3** (10%).

Method 4: Triaquatricarbonylrhodium bromide (31.0 mg, 76.7 μmol) was added to an aqueous solution (1.0 mL) of **1** (14.9 mg, 76.7 μmol) in a microwave vial (5.0 mL). The reaction vial was crimp-sealed prior to heating in the microwave at 110°C, 17 bar (max), and 300 W (max) for 30 s with stirring. The reaction mixture was chilled, and then analyzed by LC-MS (APCI). **2** (94%), **3** (4%).

Method 5: Triaquatricarbonylrhodium bromide (30.8 mg, 76.2 μmol) was added to an aqueous solution (1.0 mL) of **1** (14.8 mg, 76.2 μmol) in a microwave vial (5.0 mL). The reaction vial was crimp-sealed prior to heating in the microwave at 110°C, 17 bar (max), and 300 W (max) for 1 min with stirring. The reaction mixture was chilled, and then analyzed by LC-MS (APCI). **2** (95%), **3** (5%).

Method 6: Same as Table 1, entry 2.

Experiment of Table 4 Method 1: Same as Table 1, entry 2.

Method 2: Triaquatricarbonylrhenium bromide (30.4 mg, 75.2 μmol) was added to a mixed solution of water and MeOH (3/1, 1.0 mL) of **1** (14.6 mg, 75.2 μmol) in a microwave vial (5.0 mL). The reaction vial was crimp-sealed prior to heating in the microwave at 110°C, 17 bar (max), and 300 W (max) for 5 min with stirring. The reaction mixture was chilled, and then analyzed by LC-MS (APCI). **2** (85%), **3** (4%).

Method 3: Triaquatricarbonylrhenium bromide (30.8 mg, 76.2 μmol) was added to a solution of water and MeOH (1/1, 1.0 mL) of **1** (14.8 mg, 76.2 μmol) in a microwave vial (5.0 mL). The reaction vial was crimp-sealed prior to heating in the microwave at 110°C, 17 bar (max), and 300 W (max) for 5 min with stirring. The reaction mixture was chilled, and then analyzed by LC-MS (APCI). **2** (85%), **3** (4%).

Method 4: Triaquatricarbonylrhenium bromide (31.2 mg, 77.2 μmol) was added to a solution of water and MeOH (1/3, 1.0 mL) of **1** (15.0 mg, 77.2 μmol) in a microwave vial (5.0 mL). The reaction vial was crimp-sealed prior to heating in the microwave at 110°C, 17 bar (max), and 300 W (max) for 5 min with stirring. The reaction mixture was chilled, and then analyzed by LC-MS (APCI). **2** (76%), **3** (5%), **4** (4%).

Method 5: Triaquatricarbonylrhenium bromide (32.5 mg, 80.3 μmol) was added to a solution of water and MeOH (1/9, 1.0 mL) of **1** (15.6 mg, 80.3 μmol) in a microwave vial (5.0 mL). The reaction vial was crimp-sealed prior to heating in the microwave at 110°C, 17 bar (max), and 300 W (max) for 5 min with stirring. The reaction mixture was chilled, and then analyzed by LC-MS (APCI). **2** (56%), **3** (13%), **4** (9%).

Experiment of Chart 2 **2** (10.4 mg, 23.8 μmol) was dissolved in MeOH (1.0 mL) in a microwave vial (5.0 mL). The reaction vial was crimp-sealed prior to heating in the microwave at 110°C, 17 bar (max), and 300 W (max) for 5 min with stirring. The reaction mixture was chilled, and then analyzed by LC-MS (APCI). **2** (95%).

Experiment of Chart 3 **3** (4.0 mg, 8.6 μmol) was dissolved in water (0.5 mL) in a microwave vial (5.0 mL). The reaction vial was crimp-sealed prior to heating in the microwave at 110°C, 17 bar (max), and 300 W (max) for 5 min with stirring. The reaction mixture was chilled, and then analyzed by LC-MS (APCI). **2** (>99%).

3 (10.4 mg, 22.4 μmol) was dissolved in MeOH (1.0 mL) in a microwave vial (5.0 mL). The reaction vial was crimp-sealed prior to heating in the microwave at 110°C, 17 bar (max), and 300 W (max) for 5 min with stirring. The reaction mixture was chilled, and then analyzed by LC-MS (APCI). **2** (45%), **3** (12%).

Synthesis of $^{99m}\text{Tc}(\text{CO})_3$ -PAMA Complex Radiochemical yields were calculated from the radioactivity peak area in the HPLC profile. After reactions, the reaction samples were purified by radio-HPLC. Then, radioactivity was dynamically plotted to obtain the radioactivity profile. We calculated (radioactivity of objective compound)/(total radioactivity) as yield of $^{99m}\text{Tc}(\text{CO})_3$ complex.

Experiment of Table 5 Method 1: Triaquatricarbonyl technetium (I) cation (6.2 MBq/50 μL) was added to an aqueous solution (150 μL) of **1** (1.0 mg, 5.12 μmol) in a microwave

vial (5.0 mL). The reaction vial was crimp-sealed prior to heating in the microwave at 110°C, 17 bar (max), and 300 W (max) for 10 s. The reaction mixture was chilled, and then analyzed by radio-HPLC. Radiochemical yield: >99%.

Method 2: Triaquatricarbonyl technetium(I) cation (6.2 MBq/50 μL) was added to an aqueous solution (150 μL) of **1** (1.0 mg, 5.12 μmol) in a microwave vial (5.0 mL). The reaction vial was crimp-sealed prior to heating in the microwave at 110°C, 17 bar (max), and 300 W (max) for 1 min. The reaction mixture was chilled, and then analyzed by radio-HPLC. Radiochemical yield: >99%.

Method 3: Triaquatricarbonyl technetium(I) cation (6.2 MBq/50 μL) was added to a solution of water and MeOH (1/2, 150 μL) of **1** (1.0 mg, 5.12 μmol) in a microwave vial (5.0 mL). The reaction vial was crimp-sealed prior to heating in the microwave at 110°C, 17 bar (max), and 300 W (max) for 1 min with stirring. The reaction mixture was chilled, and then analyzed by radio-HPLC. Radiochemical yield: >99%.

Method 4: Triaquatricarbonyl technetium(I) cation (6.2 MBq/50 μL) was added to a solution of MeOH (150 μL) of **1** (1.0 mg, 5.12 μmol) in a microwave vial (5.0 mL). The reaction vial was crimp-sealed prior to heating in the microwave at 110°C, 17 bar (max), and 300 W (max) for 1 min with stirring. The reaction mixture was chilled, and then analyzed by radio-HPLC. Radiochemical yield: 62%.

Method 5: Triaquatricarbonyl technetium(I) cation (1.2 MBq/10 μL) was added to a solution of MeOH (190 μL) of **1** (1.0 mg, 5.12 μmol) in a microwave vial (5.0 mL). The reaction vial was crimp-sealed prior to heating in the microwave at 110°C, 17 bar (max), and 300 W (max) for 1 min with stirring. The reaction mixture was chilled, and then analyzed by radio-HPLC. Radiochemical yield: 63%.

Acknowledgements We would like to thank FUJIFILM RI Pharma Co., Ltd., Tokyo, Japan, for providing IsoLink kitTM. This work was supported in part by a Grant-in-Aid for Young Scientists (B) and Exploratory Research from the Ministry of Education, Culture, Sports, Science and Technology of Japan.

References

- 1) Jurisson S. S., Lydon J. D., *Chem. Rev.*, **99**, 2205–2218 (1999).
- 2) Arano Y., *Ann. Nucl. Med.*, **16**, 79–93 (2002).
- 3) Schibli R., Schubiger P. A., *Eur. J. Nucl. Med.*, **29**, 1529–1542 (2002).
- 4) Shestopalov A. M., Fedorov A. E., Rodinovskaya L. A., Shestopalov A. A., Gakh A. A., *Tetrahedron Lett.*, **50**, 5257–5259 (2009).
- 5) Causey P. W., Besanger T. R., Schaffer P., Valliant J. F., *Inorg. Chem.*, **47**, 8213–8221 (2008).
- 6) Green A. E. C., Causey P. W., Louie A. S., Armstrong A. F., Harrington L. E., Valliant J. F., *Inorg. Chem.*, **45**, 5727–5729 (2006).
- 7) Schibli R., La Bella R., Alberto R., Garcia-Garayoa E., Ortner K., Abram U., Schubiger P. A., *Bioconjug. Chem.*, **11**, 345–351 (2000).
- 8) Banerjee S. R., Levadala M. K., Lazarova N., Wei L., Valliant J. F., Stephenson K. A., Babich J. W., Maresca K. P., Zubieta J., *Inorg. Chem.*, **41**, 6417–6425 (2002).
- 9) Mundwiler S., Candrea L., Häfliger P., Ortner K., Alberto R., *Bioconjug. Chem.*, **15**, 195–202 (2004).
- 10) Lazarova N., James S., Babich J., Zubieta J., *Inorg. Chem. Commun.*, **7**, 1023–1026 (2004).

Development of Novel Nanocarrier-Based Near-Infrared Optical Probes for *In Vivo* Tumor Imaging

Yoichi Shimizu · Takashi Temma · Isao Hara ·
Ryo Yamahara · Ei-ichi Ozeki · Masahiro Ono ·
Hideo Saji

Received: 5 September 2011 / Accepted: 18 October 2011 / Published online: 10 November 2011
© Springer Science+Business Media, LLC 2011

Abstract Optical imaging with near-infrared (NIR) fluorescent probes is a useful diagnostic technology for *in vivo* tumor detection. Our plan was to develop novel NIR fluorophore-micelle complex probes. IC7-1 and IC7-2 were synthesized as novel lipophilic NIR fluorophores, which were encapsulated in an amphiphilic polydepsipeptide micelle “lactosome”. The fluorophore-micelle complexes IC7-1 lactosome and IC7-2 lactosome were evaluated as NIR fluorescent probes for *in vivo* tumor imaging. IC7-1 and IC7-2 were synthesized and then encapsulated in lactosomes. The optical properties of IC7-1, IC7-2, IC7-1 lactosome and IC7-2 lactosome were measured. IC7-1 lactosome and IC7-2 lactosome were administered to tumor-bearing mice, and fluorescence images were acquired for 48 h. IC7-1 and IC7-2 were successfully synthesized in 12% and 6.3% overall yield, and maximum emission wavelengths in chloroform were observed at 858 nm and 897 nm, respectively. Aqueous buffered solutions of IC7-1 lactosome and IC7-2 lactosome showed similar fluorescence spectra in chloroform and higher or comparable quantum yields and higher photostability compared with ICG. Both lactosome probes specifically visualized tumor tissue 6 h post-administration. IC7-1 lactosome and IC7-2 lactosome could be promising NIR probes for *in vivo* tumor imaging.

Keywords Optical · Near-infrared · Micelle · Molecular imaging

Introduction

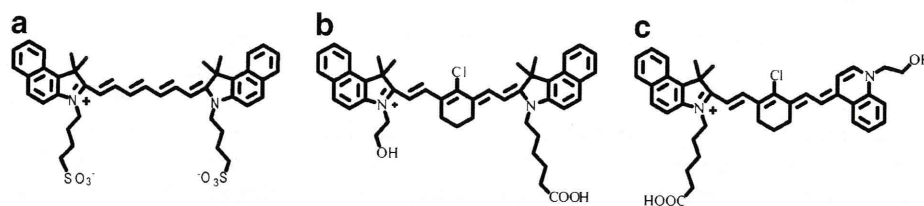
Molecular imaging is an evolving field that is progressing from basic research to use in clinical diagnosis [1, 2]. Among several imaging methods, optical imaging can conveniently and safely offer pronounced spatial and temporal resolution that is desirable for *in vivo* applications, especially in the area of cancer imaging. It is notable that near-infrared (NIR) light (700–1,000 nm) transmits deeply through tissues with low scattering, absorption, and auto-fluorescence [3, 4].

Although indocyanine green (ICG, Fig. 1a) is a NIR probe approved by the Food and Drug Administration (FDA) for monitoring cardiac function and hepatic output [5–7], its low quantum yield [4] and low stability in aqueous solution [3] are drawbacks to further applications as an *in vivo* fluorescent molecular probe. ICG derivatives with enhanced lipophilicity could help solve these problems if they were to be utilized in a lipophilic environment, but fluorescent tags for *in vivo* usage should be amenable to an aqueous environment. On the other hand, a polydepsipeptide micelle composed of polysarcosine (PSar) and poly-L-lactic acid (PLLA), named lactosome, has been reported to be an *in vivo* stable, hydrophilic nanocarrier of ~30 nm in diameter, which can encapsulate hydrophobic compounds and effectively deliver them into tumor tissue by an enhanced permeability and retention (EPR) effect with low nonspecific accumulation in the reticuloendothelial system [8, 9]. Thus, our goal was to synthesize lipophilic ICG derivatives possessing better fluorescence properties and encapsulate them in lactosomes to provide NIR probes for *in vivo* tumor imaging.

Y. Shimizu · T. Temma · M. Ono · H. Saji (✉)
Department of Patho-Functional Bioanalysis,
Graduate School of Pharmaceutical Sciences,
Kyoto University,
46-29 Yoshida Shimoadachi-cho, Sakyo-ku,
Kyoto 606-8501, Japan
e-mail: hsaji@pharm.kyoto-u.ac.jp

I. Hara · R. Yamahara · E.-i. Ozeki
Technology Research Laboratory, Shimadzu Corporation,
3-9-4 Soraku-gun, Seika-cho,
Kyoto 619-0237, Japan

Fig. 1 Chemical structures of ICG (a), IC7-1 (b) and IC7-2 (c)



To develop the novel lipophilic NIR compound, IC7-1 (Fig. 1b), a cyclohexenyl ring was introduced into the polymethine chain of ICG to rigidify the structure and to provide improved photostability and a higher quantum yield [10, 11]. A related asymmetric ICG derivative incorporating a quinoline moiety, IC7-2 (Fig. 1c), which had an elongated emission spectrum, was also synthesized for comparative purposes [12].

Materials and Methods

Materials

Aniline, cyclohexanone, N,N'-dicyclohexylcarbodiimide, sodium hydride, 6-bromohexanoic acid, potassium iodide, sodium acetate, 2-iodoethanol, N-hydroxysuccinimide, N,N-dimethylformamide, and ethanol were purchased from Wako Pure Chemical Industries, Ltd. 1,1,2-Trimethylbenz[e]indole was purchased from Sekisui Medical CO, Ltd. ICG was purchased from Tokyo Chemical Industry Co, Ltd.

Instruments

UV-vis spectra were measured using a UV-1800 (SHIMADZU Corporation, Kyoto, Japan). Mass spectra were acquired on a SHIMADZU LC-MS2010 EV (SHIMADZU Corporation, Kyoto, Japan) and an Axima-CFR plus (SHIMADZU Corporation, Kyoto, Japan). ¹H-NMR spectra were recorded on a JEOL ECP-300 (JEOL Ltd., Tokyo, Japan). Fluorescence spectroscopy was performed with a Fluorolog-3 (HORIBA Jobin Yvon Inc., Kyoto, Japan), using a slit width of 5 nm for both excitation and emission measurements.

Synthesis

N-[5-Anilino-3-chloro-2,4-(propane-1,3-diyl)-2,4-pentadiene-1-ylidene]anilinium Chloride (1)

Phosphorus oxychloride (11 mL, 0.12 mol) was added dropwise to anhydrous DMF (13 mL, 0.17 mol) at 0 °C. After 1 h, cyclohexanone (5.5 mL, 0.053 mol) was added,

and the mixture was refluxed for 1 h. After cooling to rt, an aniline/EtOH [1:1 (v/v), 18 mL] mixture was added dropwise, and the reaction was continued at rt for 30 min. The mixture was poured into ice cold H₂O/HCl (10:1, 110 mL), and the resulting residue was filtered, washed with cold H₂O and THF, and then dried *in vacuo* to obtain compound **1** (10.2 g, 53.6%); ¹H NMR (DMSO-*d*₆, 300 MHz) δ8.54 (s, 2H), 7.6-7.2 (m, 10H), 2.74 (t, 4H), 1.85 (m, 2H).

3-(5-Carboxy-pentyl)-1,1,2-trimethyl-1H-benz[e]indolium iodide (2)

6-Bromohexanoic acid (8.4 g, 43.0 mmol) and potassium iodide (7.2 g, 43 mmol) were dissolved in toluene (5 mL). After addition of 1,1,2-trimethyl-1H-benz[e]indole (3.0 g, 14.3 mmol), the mixture was refluxed for 15 h. The resulting precipitate was washed with THF, chilled H₂O, and chloroform and then dried *in vacuo* to obtain compound **2** (5.0 g, 77%); ¹H NMR (CD₃OD) 8.33 (d, 1H, J=8.5), 8.24 (d, 1H, J=8.8), 8.16 (d, 1H, J=8.3), 8.02 (d, 1H, J=8.8), 7.8 (t, 1H, J=7.2), 7.71 (t, 1H, J=7.2), 4.64 (t, 2H, J=7.7), 2.35 (t, 2H, J=6.9), 2.0-1.9 (m, 2H), 1.84 (s, 6H), 1.75-1.65 (m, 2H), 1.65-1.55 (m, 2H).

2-[4'-Chloro-6'-(*N*-phenyl)-3',5'-trimethyleneheptatrien-1-yl]-1-(5-Carboxy-pentyl)-1,1,2-trimethyl-1H-benz[e]indolium iodide (3)

A mixture of compound **1** (3.00 g, 8.35 mmol), **2** (3.77 g, 8.35 mmol) and anhydrous sodium acetate (0.753 g, 9.19 mmol) in anhydrous EtOH (75 mL) was refluxed for 6 h under a N₂ atmosphere. After the reaction was complete, the mixture was neutralized with 0.2 M phosphate buffer (pH 7.0), and then extracted with chloroform. The extract was evaporated, and the residue was purified by column chromatography to obtain compound **3** (1.45 g, 25.5%); ¹H NMR (CD₃OD) δ8.56 (s, 1H), 8.2-8.1 (m, 2H), 7.95-7.85 (m, 2H), 7.6-7.1 (m, 8H), 6.10 (d, 1H, J=13.8), 4.17 (t, 2H, J=7.2), 2.71 (t, 4H, J=5.8), 2.27 (t, 2H, J=7.4), 2.0-1.8 (m, 4H), 1.93 (s, 6H), 1.8-1.6 (m, 2H), 1.6-1.4 (m, 2H); MS (ESI, pos.) *m/z* calcd for C₃₅H₃₈ClN₂O₂ 554 (M⁺), found 554.

3-(2-Hydroxyethyl)-1,1,2-trimethyl-1H-benz[e]indolium iodide (4)

1,1,2-Trimethyl-1H-benz[e]indole (2.0 g, 9.556 mmol) was dissolved in dry toluene (10 mL) at 80 °C under a N₂ atmosphere. To the solution was added 2-iodoethanol (1.64 g, 9.556 mmol), and the mixture was refluxed for 2 h. After cooling to rt, a slightly blue residue was collected, washed with toluene, and then dried *in vacuo* to obtain compound **4** (1.21 g, 33%); ¹H NMR (DMSO-d₆) δ8.39 (d, 1H, J=8.0), 8.29 (d, 1H, J=8.8), 8.22 (d, 1H, J=8.0), 8.14 (d, 1H, J=9.1), 7.79 (t, 1H, J=7.2), 7.73 (t, 1H, J=6.9), 4.72 (t, 2H, J=4.7), 3.94 (t, 2H, J=4.7), 2.93 (s, 3H), 1.78 (s, 6H).

1-(2-Hydroxyethyl)-4-methylquinolinium iodide (5)

A mixture of 4-methylquinoline (1 g, 7 mmol) and 2-iodoethanol (1.2 g, 7 mmol) in dry toluene (5 mL) was stirred at 80 °C under a N₂ atmosphere for 4 h. After cooling, a yellow residue was collected, washed with toluene, and then dried *in vacuo* to obtain compound **5** (1.63 g, 74%); ¹H NMR (CD₃OD) δ9.14 (d, 1H, J=6.3), 8.62–8.52 (m, 2H), 8.25 (t, 1H, J=6.3), 8.06 (t, 1H, J=6.2), 7.97 (d, 1H, J=6.0), 5.14 (t, 2H, J=4.9), 4.08 (t, 2H, J=5.0), 3.07 (s, 3H).

2-[4'-Chloro-7'-(1''-(2-Hydroxyethyl)-1,1,2-trimethyl-1H-benz[e]indolium)-3',5'-trimethyleneheptatrien-1-yl]-1-(5-Carboxypentyl)-1,1,2-trimethyl-1H-benz[e]indolium iodide (IC7-1)

A mixture of compound **3** (1.16 g, 1.70 mmol), **4** (0.714 g, 1.87 mmol), and anhydrous sodium acetate (0.153 g, 1.87 mmol) in anhydrous EtOH (29 mL) was refluxed for 5 h under a N₂ atmosphere. After the reaction was complete, the mixture was neutralized with 0.2 M phosphate buffer (pH 7.0) and then extracted with chloroform. The organic extract was evaporated, and the residue was purified by column chromatography to obtain IC7-1 (1.22 g, 85.3%); ¹H NMR (CD₃OD) δ8.54 (m, 2H), 8.26 (t, 2H, J=8.1), 8.05–7.95 (m, 4H), 7.7–7.4 (m, 6H), 6.46 (d, 1H, J=14.3), 6.28 (d, 1H, J=14.0), 4.42 (t, 2H, J=5.0), 4.28 (t, 2H, J=8.0), 4.03 (t, 2H, J=5.0), 2.75 (t, 4H, J=5.8), 2.31 (t, 2H, J=7.2), 2.1–1.8 (m, 6H), 2.05 (s, 6H), 2.01 (s, 6H), 1.8–1.6 (m, 2H), 1.6–1.4 (m, 2H): MS (ESI, pos) m/z calcd for C₄₆H₅₀ClN₂O₃ 714 (M⁺), found 714.

IC7-1-NHS

To a solution of IC7-1 (600 mg, 0.713 mmol) in anhydrous DMF (12 mL) was added dicyclohexylcarbodiimide (DCC, 440 mg, 2.14 mmol) at 0 °C. The reaction was stirred for

20 min, and then N-hydroxysuccinimide (NHS, 246 mg, 2.14 mmol) was added. The solution was gradually allowed to warm to room temperature, and it was stirred for 2 days. After the reaction was complete, ethyl acetate was added to the mixture, and the dicyclohexylurea was removed by filtration. The solution was evaporated, and the residue was purified by flash chromatography to obtain IC7-1-NHS (100 mg, 14.9%); ¹H NMR (CD₃OD) δ8.50 (m, 2H), 8.23 (t, 2H, J=8.1), 8.1–7.9 (m, 4H), 7.7–7.4 (m, 6H), 6.45 (d, 1H, J=14.3), 6.24 (d, 1H, J=14.3), 4.41 (t, 2H, J=5.0), 4.24 (t, 2H, J=8.0), 4.03 (t, 2H, J=4.9), 2.8–2.6 (m, 6H), 2.78 (s, 4H), 2.0–1.5 (m, 8H), 2.01 (s, 6H), 1.99 (s, 6H): MS calcd for C₅₀H₅₃ClN₃O₅ (M⁺) 811, found 811.

2-[4'-Chloro-7'-(1''-(2-Hydroxyethyl)-4-methylquinolinium)-3',5'-trimethyleneheptatrien-1-yl]-1-(5-Carboxypentyl)-1,1,2-trimethyl-1H-benz[e]indolium iodide (IC7-2)

A mixture of compound **3** (414 mg, 0.608 mmol), **5** (210.7 mg, 0.669 mmol), and anhydrous sodium acetate (54.9 mg, 0.669 mmol) in anhydrous EtOH (12 mL) was refluxed for 8 h under a N₂ atmosphere. After the reaction was complete, the mixture was neutralized with 0.2 M phosphate buffer (pH 7.0) and then extracted with chloroform and methanol. The organic extract was evaporated, and the residue was purified by column chromatography to obtain IC7-2 (221 mg, 46.7%); ¹H NMR (CD₃OD) δ8.65 (d, 1H, J=6.6), 8.57 (d, 1H, J=8.8), 8.39 (d, 1H, J=15.1), 8.26 (d, 1H, J=8.8), 8.15–7.65 (m, 7H), 7.44 (t, 1H, J=7.4), 7.35–7.1 (m, 3H), 5.69 (d, 1H, J=13.4), 4.05 (t, 2H, J=4.7), 3.83 (t, 2H, J=6.9), 2.8–2.65 (m, 4H), 2.21 (t, 2H, J=7.4), 1.90 (s, 6H), 2.0–1.6 (m, 7H), 1.6–1.2 (m, 3H): MS (ESI, pos) m/z calcd for C₄₁H₄₄ClN₂O₃ (M⁺) 647, found 647.

IC7-2-NHS

To a solution of IC7-2 (355 mg, 0.457 mmol) and NHS (157.7 mg, 1.370 mmol) in anhydrous DMF (3.5 mL) was added DCC (188.5 mg, 0.914 mmol), and the mixture was stirred for 1 h at 0 °C. The solution was allowed to gradually warm to room temperature, and it was stirred for 2.5 days. After the reaction was complete, ethyl acetate was added to the mixture, and the dicyclohexylurea was removed by filtration. The filtrate was evaporated, and the residue was purified by flash chromatography to obtain IC7-2-NHS (62 mg, 15.6%); ¹H NMR (CD₃OD) δ8.64 (d, 1H, J=6.6), 8.56 (d, 1H, J=8.5), 8.34 (d, 1H, J=12.4), 8.25 (d, 1H, J=8.8), 8.15–7.65 (m, 7H), 7.44 (t, 1H, J=7.4), 7.35–7.1 (m, 3H), 5.69 (br, 1H), 4.04 (t, 2H, J=4.7), 3.83 (br, 2H), 2.66 (s, 4H), 2.9–2.50 (m, 6H), 1.90 (s, 6H), 2.0–1.6 (m, 7H), 1.6–1.2 (m, 3H): MS (ESI, pos) m/z calcd for C₄₅H₄₇ClN₃O₅ (M⁺) 744, found 744.

Preparation of IC7-1 or IC7-2 encapsulated lactosomes

To a solution of IC7-1-NHS (1.1 mg, 1.68 μmol) or IC7-2-NHS (1.0 mg, 1.68 μmol) in anhydrous DMF (1 mL) was added PLLA₃₀ bearing a free amino group (3.45 mg, 1.52 μmol). The solution was stirred at room temperature overnight while shielding the reaction from light, and the resulting mixture was purified by size exclusion chromatography (Sephadex LH-20 column) using DMF as eluant. The fraction of high molecular mass was collected and dried *in vacuo*. IC7-1-PLLA: MS (MALDI-TOF, pos) *m/z* calcd for C₅₀H₅₃CIN₃O₅ ([M+H]⁺) 2958, found 2958. IC7-2-PLLA: MS (MALDI-TOF, pos) *m/z* calcd for C₁₃₅H₁₇₂CIN₄O₆₃ (M⁺) 2895, found 2895.

The amphiphilic polymer PLLA₃₀-block-PSar₇₀ (Fig. 2) was supplied by the Shimadzu Corporation. A chloroform (1 mL) solution of the polymer (388 nmol) and IC7-1-PLLA (3.9 nmol) or IC7-2-PLLA (3.9 nmol) was dripped into a glass test tube. The solvent was removed under reduced pressure to form a thin film on the walls of the tube. PBS buffer (0.1 M, pH 7.4) was added to the test tube, and the tube was heated at 82 °C for 20 min. The resulting aqueous solution was filtered through a 0.20 μm Acrodisc® syringe filter (Pall Corp, East Hills, NY). The size distribution of IC7-1 lactosome and IC7-2 lactosome was measured at 25 °C using a Zetasizer Nano-S90 (Malvern instruments Ltd., UK). The purities of IC7-1 lactosome and IC7-2 lactosome were measured by size exclusion chromatography using a Superdex 200 10/300 GL column (GE Healthcare, U.K.) equilibrated with PBS (–) at a flow rate of 0.5 ml/min. Absorbances at 215 nm and 830 nm were used for detection of the lactosome and IC7-1/IC7-2, respectively.

Optical characteristics of IC7-1, IC7-1 lactosome, IC7-2 and IC7-2 lactosome

The log P values of IC7-1, IC7-2, and ICG were calculated by ACD/Labs ver. 11.0 (Advanced Chemistry Development, Inc., Toronto, Canada).

The fluorescence emission spectra of IC7-1 and IC7-2 (10 μM) were measured in methanol and chloroform at 25 °C, following excitation at 815 nm and 820 nm, respectively. Fluorescence emission spectra of IC7-1 lactosome and IC7-2 lactosome (1.3 μM) were measured

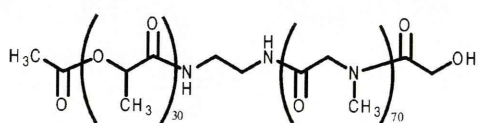


Fig. 2 Chemical structure of the amphiphilic block polymer (PLLA₃₀-block-PSar₇₀)

in H₂O at 25 °C, following excitation at 815 nm and 820 nm, respectively. Quantum yields for IC7-1, IC7-1 lactosome, IC7-2, and IC7-2 lactosome were acquired by a sphere accessory equipped with a Fluorolog-3 (HORIBA Jobin Yvon Inc., Kyoto, Japan). Excitation spectra of IC7-1 and IC7-2 (10 μM) were measured in methanol and chloroform at 25 °C following emission at 880 nm and 900 nm, respectively, and those of IC7-1 lactosome and IC7-2 lactosome (1.3 μM) were measured in H₂O at 25 °C following excitation at 880 nm and 890 nm, respectively. Absorption spectra of IC7-1 and IC7-2 (10 μM) were measured in methanol and chloroform at 25 °C, and those of IC7-1 lactosome and IC7-2 lactosome were measured in water at 25 °C.

The photostability of IC7-1 lactosome, IC7-2 lactosome, and ICG were evaluated by a decrease of absorbance over time. IC7-1 lactosome (1.3 μM in H₂O), IC7-2 lactosome (1.3 μM in H₂O) and ICG (1.3 μM in H₂O) were continuously illuminated with a tungsten lamp in a visible-ultraviolet spectrophotometer (UV-1800) for 1 h. The absorption was measured at the corresponding wavelengths (IC7-1 lactosome: 830 nm, IC7-2 lactosome: 830 nm, and ICG: 780 nm) every 0.1 min for 1 h after UV illumination was initiated.

Tumor bearing mice

Female nude mice (BALB/c nu/nu) supplied by Japan SLC, Inc. (Hamamatsu, Japan), were housed under a 12-h light/12-h dark cycle and were given free access to food and water. Animal experiments in this study were conducted in accordance with institutional guidelines and were approved by the Kyoto University Animal Care Committee, Japan. FM3A cells were supplied by the Health Science Research Resources Bank (HSRRB) (Osaka, Japan). The cell lines were cultured in DMEM medium with 10% fetal bovine serum at 37 °C in a humidified atmosphere containing 5% CO₂. FM3A cells, 5 × 10⁶ cells in 100 μL of phosphate-buffered saline (PBS), were subcutaneously inoculated into the right hind legs of 7-week-old nude mice. Tumor bearing mice 12 days after transplantation were used for the imaging study.

In vivo imaging study

IC7-1 lactosome and IC7-2 lactosome (1.7 μM , 200 μL) were injected into groups of three tumor-bearing mice, and NIRF images were obtained using a Clairvivo OPT (SHIMADZU Corporation, Kyoto, Japan) with a 785 nm single laser (IC7-1 lactosome) or 808 nm single laser (IC7-2 lactosome) for excitation and a 845/55 nm band-path filter (IC7-1 lactosome) or 850 nm long-path filter (IC7-2 lactosome) for emission. During the imaging process, mice

were kept on the imaging stage under anesthesia using a 2.5% isoflurane gas in oxygen flow (1.5 L/min). For image analysis, Clairvivo OPT measurement and display software ver. 2.00 (SHIMADZU Corporation, Kyoto, Japan) was used. Regions of interest (ROI) were designated for the tumor and muscle (the left hind leg) on the back images and for the liver on the front images. The average signal intensity values were recorded for each ROI and were plotted versus time.

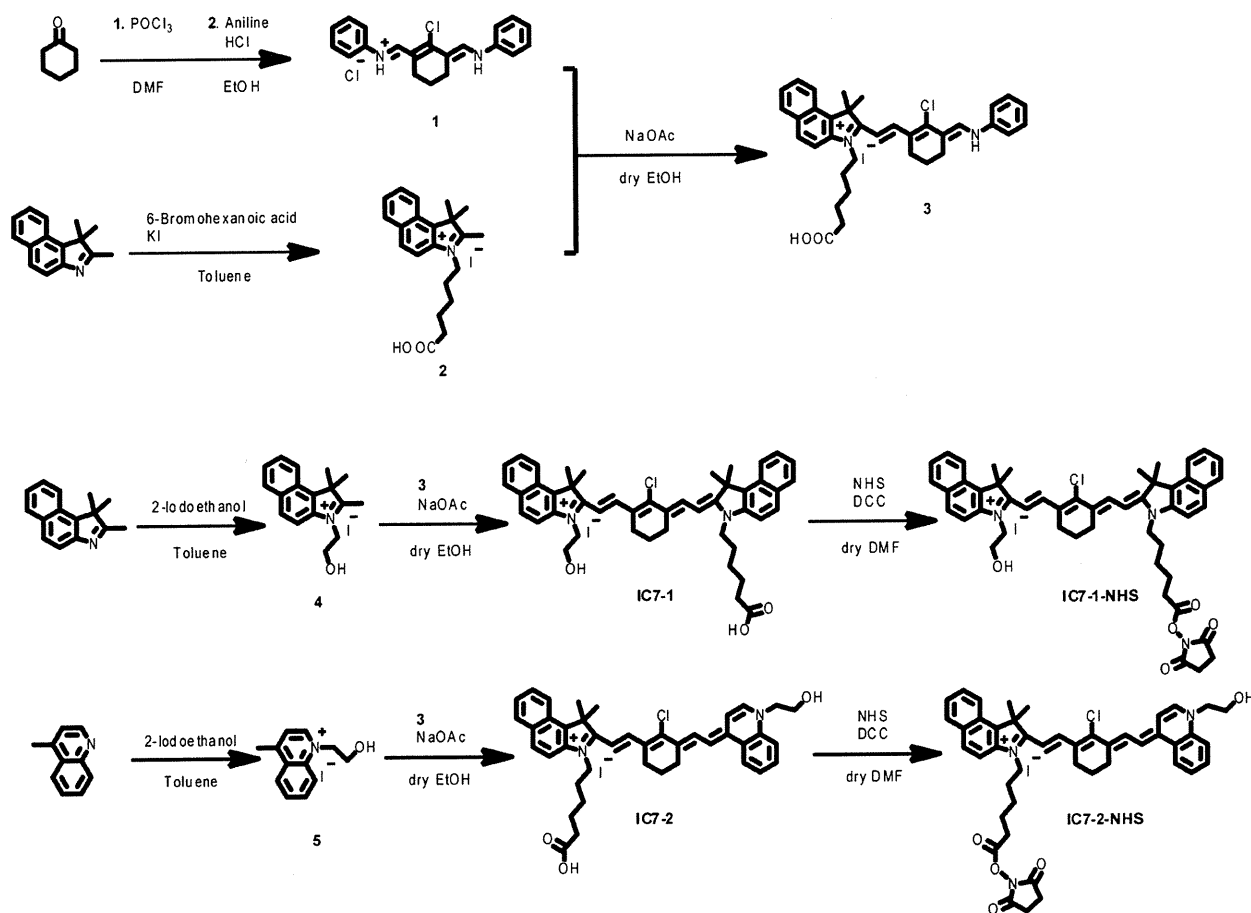
Statistics

Data are presented as means±S.D. Statistical analysis of the photostability of IC7-1 lactosome and IC7-2 lactosome vs ICG was performed with two-way factorial ANOVA followed by the Tukey-Kramer test. Statistical analyses for fluorescence intensities of tumor vs muscle or liver of mice administered IC7-1 lactosome or IC7-2 lactosome were performed with two-way factorial ANOVA followed by the Tukey-Kramer test.

Results

Synthesis of IC7-1, IC7-2, IC7-1 lactosome and IC7-2 lactosome

IC7-1 and IC7-2 were synthesized from cyclohexanone and 1,1,2-trimethyl-1*H*-benz[e]indole, as shown in Scheme 1, in 12% and 6.3% overall yield. The calculated log *P* values of IC7-1 and IC7-2 were 3.62 and 0.90, respectively, while the clog *P* of ICG was −1.69. To allow these fluorophores to dissolve in aqueous solvent, they were encapsulated in lactosomes using a film rehydration technique. The preparation of IC7-1 lactosome and IC7-2 lactosome was confirmed by size exclusion chromatography using Superdex 200 10/300 GL (GE Healthcare, U.K.), and dual absorbance peaks at 280 nm (lactosome) and 830 nm (IC7-1/IC7-2) were only seen in the higher molecular weight fraction (4–5 min). The particle sizes of IC7-1 lactosome and IC7-2 lactosome were 33.4±3.1 nm (*n*=6) and 39.6±1.9 nm (*n*=4), respectively.



Scheme 1 Synthetic scheme for the preparation of IC7-1, IC7-2 and NHS derivatives

Fluorescence characteristics of IC7-1, IC7-2, IC7-1 lactosome and IC7-2 lactosome

IC7-1, a lipophilic fluorophore with a cyclohexene ring in the interior of the polymethine chain of the ICG structure, had a maximum emission wavelength at 858 nm in chloroform (Table 1). IC7-2 with an unsymmetrical cyanine structure had a maximum emission wavelength at 897 nm in chloroform, which as expected was a longer emission wavelength compared with conventional NIR-dyes. In addition to maximum emission wavelength, other fluorescent properties of IC7-1 and IC7-2 in chloroform such as fluorescence spectrum, quantum yield, and extinction coefficient were also quite similar to those of IC7-1 lactosome and IC7-2 lactosome measured in water (Fig. 3, Table 1). In particular, IC7-1 and IC7-1 lactosome had sharp absorbance and emission spectra and a narrow Stokes shift, while IC7-2 and IC7-2 lactosome had broad absorption spectra and a relatively long Stokes shift.

The fluorescence characteristics of IC7-1, IC7-1 lactosome, IC7-2, and IC7-2 lactosome were compared with ICG as summarized in Table 1. Both IC7-1 and IC7-2 displayed longer absorbance, excitation, and emission wavelengths than ICG. IC7-1 and IC7-2 had higher quantum yields and molar extinction coefficients in chloroform than in methanol. IC7-1 lactosome had approximately 52 nm and 43 nm longer maximum absorbance and emission wavelengths and approximately 2.5 fold higher quantum yield and molar extinction coefficients compared with ICG. IC7-2 lactosome had a maximum emission wavelength that was 55 nm longer than IC7-1 lactosome and 98 nm longer than ICG.

Regarding photostability of the three probes, the absorbances of IC7-1 lactosome and IC7-2 lactosome were stable for 1 h under tungsten lamp irradiation (Fig. 4). On the other hand, the absorbance of ICG significantly decreased in a time-dependent manner ($p < 0.0001$), and the normalized absorbance of ICG after 60 min was 61% of the 0 min value.

In vivo imaging study

Fluorescence images of tumor-bearing mice administered IC7-1 lactosome or IC7-2 lactosome are shown in Fig. 5a and b, respectively. The tumors of mice administered IC7-1 lactosome and IC7-2 lactosome were visible with both agents 6 h after administration. The fluorescence intensity at the tumor region of mice administered IC7-1 lactosome (Fig. 5c) and IC7-2 lactosome (Fig. 5d) gradually increased in a time-dependent manner reaching a peak 24 h after administration that was significantly greater than the fluorescence observed in the muscle and liver regions ($p < 0.05$). The fluorescence intensities of tumors 24 h after probe administration were 3.1 fold (IC7-1 lactosome) and 2.5 fold (IC7-2 lactosome) greater than those at the 0 h time point (immediately after probe administration). The intensities in the muscle region (the opposite side from the tumor) were relatively constant during the study, and the tumor-to-muscle fluorescence ratios 24 h after administration were 2.2 ± 0.7 (IC7-1 lactosome) and 2.2 ± 0.2 (IC7-2 lactosome). The tumor-to-liver fluorescence ratios 24 h after administration were 2.5 ± 0.6 (IC7-1 lactosome) and 1.7 ± 0.2 (IC7-2 lactosome), while the intensities in the liver region of the IC7-2 lactosome group were transiently high during the early imaging phase.

Discussion

In this study, two lipophilic NIR fluorescent agents, IC7-1 and IC7-2, were prepared and evaluated (Fig. 1). To enhance the utility of these agents for *in vivo* NIR optical tumor imaging, they were encapsulated in a lactosome formulation to take advantage of the ability of lactosomes to effectively target and deliver lipophilic compounds to tumor tissues. As expected, these fluorescent probes and their lactosome complexes displayed absorption, excitation, and emission spectra with red shifts (Fig. 3) as well as high photostability compared with ICG (Fig. 4). The IC7-1

Table 1 Optical properties of IC7-1, IC7-1 lactosome, IC7-2, IC7-2 lactosome, and ICG

Entry	Solvent	Abs _{max}	Ex _{max}	Em _{max}	Quantum yield	Extinction coefficient (M ⁻¹ cm ⁻¹)
IC7-1	CHCl ₃	829	830	858	0.054	2.1×10^5
	MeOH	819	823	840	0.021	1.2×10^5
IC7-1 lactosome	H ₂ O	831	831	850	0.059	2.2×10^5
IC7-2	CHCl ₃	781	805	897	0.008	9.2×10^4
	MeOH	790	883	932	0.001	2.6×10^4
IC7-2 lactosome	H ₂ O	830	844	905	0.014	6.0×10^4
ICG	H ₂ O	779	762	807	0.023	7.8×10^4